SANDIA REPORT

SAND2017-13359
Unlimited Release
Printed December 2017

Validation and Verification of Multi-Material Split Rings

Alexander A. Hanson, Stacy M. Nelson, Alyssa J. Skulborstad, Brian T. Werner, Timothy M. Briggs

Prepared by
Sandia National Laboratories
Albuquerque, New Mexico 87185 and Livermore, California 94550

Sandia National Laboratories is a multimission laboratory managed and operated by National Technology and Engineering Solutions of Sandia, LLC., a wholly owned subsidiary of Honeywell International, Inc., for the U.S. Department of Energy's National Nuclear Security Administration under contract DE-NA0003525.

Sandia National Laboratories

Issued by Sandia National Laboratories, operated for the United States Department of Energy by National Technology and Engineering Solutions of Sandia, LLC.

Available to DOE and DOE contractors from
U.S. Department of Energy
Office of Scientific and Technical Information
P.O. Box 62
Oak Ridge, TN 37831

Telephone: (865) 576-8401
Facsimile: (865) 576-5728
E-Mail: reports@adonis.osti.gov
Online ordering: http://www.osti.gov/bridge

Available to the public from
U.S. Department of Commerce
National Technical Information Service
5285 Port Royal Rd
Springfield, VA 22161

Telephone: (800) 553-6847
Facsimile: (703) 605-6900
E-Mail: orders@ntis.fedworld.gov
Online ordering: http://www.ntis.gov/help/ordermethods.asp?loc=7-4-0#online

SAND2017-13359
Unlimited Release
Printed December 2017

Validation and Verification of Multi-Material Split Rings

Alexander A. Hanson
Stacy M. Nelson
Alyssa J. Skulborstad
Brian T. Werrner
Timothy M. Briggs

Abstract

Process induced residual stresses commonly occur in composite structures composed of dissimilar materials. These residual stresses form due to differences in the composite materials' coefficients of thermal expansion as well as the shrinkage upon cure exhibited by most thermoset polymer matrix materials. Depending upon the specific geometric details of the composite structure and the materials' curing parameters, it is possible that these residual stresses can result in interlaminar delamination and fracture within the composite as well as plastic deformation in the structure's metallic materials. It is important to consider potential residual stresses when designing composite parts and their manufacturing processes. However, the experimental determination of residual stresses in prototype parts can be prohibitive, both in terms of financial and temporal costs. As an alternative to physical measurement, it is possible for computational tools to be used to quantify potential residual stresses in composite prototype parts. A simplified method for simulating residual stresses was previously validated with two simple bi-material structures. Continuing on, the objective of this study is to further validate the simplified method for simulating residual stresses for bi-material split rings of different composites and layup variations. The validation process uses uncertainty quantification to develop a distribution of possible simulated residual stress states that are compared to experimentally measured residual stress states of fabricated structures similar to those simulated. The results of the comparisons indicate that the proposed finite element modeling approach is capable of accurately simulating the formation of residual stresses in composite structures and a temperature independent material model is adequate within the composite's glassy region.

Acknowledgment

The authors are grateful to Helena Jin of Sandia National Laboratories for conducting the necessary experiments to determine the temperature dependence of the mechanical properties for the composite materials used in this investigation. Additionally, the authors would like to thank Corinne Hagan and Paul Suarez for their assistance in fabricating the composite layups, as well as Brian Holliday for the machining of the split rings from the cylinders.

Contents

List of Figures

List of Tables

Chapter 1

Introduction

Residual stresses in composite structures developed during the curing process, especially at the interface with another material, can lead to delamination or failure of the composite. Experiments can be done to determine the residual stress of a component; however, these are costly and difficult depending on the geometry of the component. As an alternative, validated computer simulations can be used to predict the residual stress and subsequent failure of a component. This represents a potential cost and time savings in the design process of components including composite materials.

There is a wide range of models than can be used to predict residual stresses in structures containing composite materials. The complexity of these models range from the simplest given by the analytical solution of Timoshenko to full process modeling that includes temperature dependence of materials and cure kinetics [1–7]. While the analytical equation presented by Timoshenko works reasonably well, it is limited in its application to one-dimensional, uniform and constant materials, and small strain [1]. Jumbo et. al. converts Timoshenkos equation to two dimensions by replacing the elastic moduli with the corresponding bi-axial moduli; however, the equations are still limited to uniform materials and small strain [2]. Neither application can account for polymer shrinkage a non-negligible factor in determining residual stresses in thermoset polymers. Since cure kinetics of a thermoset polymer composite can be quite impactful to the residual stress seen in a composite, White and Hahn developed a process modeling approach for composites [3, 4]. The process model follows the temperature history of the composite and follows the transition of a composite from its uncured to cured state. Expanding upon the principles of process modeling of composites, Tavakol et. al. developed a three-dimensional coupled thermomechanical process model that determines the mechanical properties on an element based on the temperature and cure kinetics (i.e. degree of cure) [5]. A similar process was also used by Volk et. al. to predict the residual stresses in various geometries [6, 7]. Full process modeling of thermoset polymer composites often requires many input parameters to fully define the cure kinetics, thermal, and mechanical properties, which may be difficult or costly to obtain.

In order to reduce the number of parameters, a simplified approach may be used to predict residual stresses, at the cost of no longer containing the necessary information to predict more complex phenomena, such as creep. The simplified approach uses one experimentally defined parameter, the stress free temperature, to account for the effects of cure kinetics and polymer shrinkage and accounts for the remainder of the residual stress with coefficients of

thermal expansion. Jumbo et. al. applied this approach to bi-material strips comprised of metals and neat resins (both isotropic materials) and Hanson et. al. further applied the method to bi-material geometries with orthotropic composites [2, 8]. Both studies showed acceptable results when compared to the experiments and Jumbo et. al. concluded that temperature dependent material properties and the inclusion of geometric non-linearity was necessary to capture the bending of the bi-material strips.

Continuing the validation of the simplified approach with orthotropic composites, the objective of this study is to determine effectiveness of the approach with other composite materials, orientations, and temperature dependent material properties. Specifically, a carbon fiber/epoxy and aluminum split ring will be investigated with two different ply orientations as well as a glass fiber/epoxy and aluminum split ring. Furthermore, a temperature dependent material model will be compared to a temperature independent material model for each investigation in order to down select an approach to use in quantifying the uncertainty of the simulations. The uncertainty quantification of the simulations will develop a distribution of possible residual stress states of the split ring based on the uncertainty of input parameters (determined through experiments or via literature). These distributions will then be compared to the experiments to continue to evaluate the viability of the simplified approach to modeling residual stresses.

Chapter 2

Experimentation

In order to validate any finite element model simulation, having real-world data from experiments is not only important, but necessary. In the case of residual stresses, choosing an experiment where the residual stresses would manifest as displacements that are visible and easily measurable was the driving force behind the bi-material split ring design. The following sections describe the manufacturing and measurement of three different bi-material split rings, representing different materials and ply orientations.

2.1 Geometry and Materials

The aluminum layer of the bi-material split ring was fabricated from a 304.8 mm) section of 6063-T6 number 4, schedule 10 pipe, which has a nominal outer diameter of 114.3 mm and wall thickness of 3.048 mm. The inner diameter of pipe is not a specified dimension, however it can be calculated to be 108.204 mm. The nominal thickness of 3.048 mm results in a stiff aluminum layer; therefore, the thickness was reduced by machining the outer diameter to 112.268 mm $\pm$ 2.54 mm, resulting in a new nominal thickness of 2.032 mm.

A carbon fiber/epoxy composite and a glass fiber/epoxy composite were considered for the bi-material split ring. Both composites are comprised of 8-harness satin (8HS) weave architecture and preimpregnated with TCR 3362 resin. The carbon fiber weave consists of 3K AS4C fiber tows, and is configured into an approximate 200 g/m^2 fabric, while the glass system uses E-glass fibers and is weaved into an approximate 300 g/m^2 fabric. The composite stack sequence comprised of four plies for the carbon fiber composite and six plies for the glass fiber composite, both laid up symmetrically with respect to the mid plane. A total of three composite/ply orientation combinations were fabricated: carbon fiber with the warp direction orientated about the circumference (no skew), glass fiber with the warp direction orientated about the circumference (no skew), and carbon fiber with the warp direction skewed 45°.

In preparation for co-bonding the composite to the aluminum, the aluminum surface was phosphoric acid anodized (PAA) and then primed with Hysol 2000. Previous bi-material experiments that excluded priming the aluminum surface resulted in de-bonding of the materials over time due to the residual stresses. Then the laminates were laid by hand from

pre-cut ply kits (203.2 mm wide and long enough to cover the circumference of the aluminum cylinder) made using a 4-axis CNC ply cutter to control geometry and fiber orientation (Figure 2.1). The bi-material cylinders were cured using standard practices of caul plates (in this case, comprised of silicon in order to wrap around the cylinder), release films, bleeder, and edge string bleeder to adequately consolidate and devolatilize the laminate during cure. The composites were cured within an autoclave at 176.7°C for four hours.

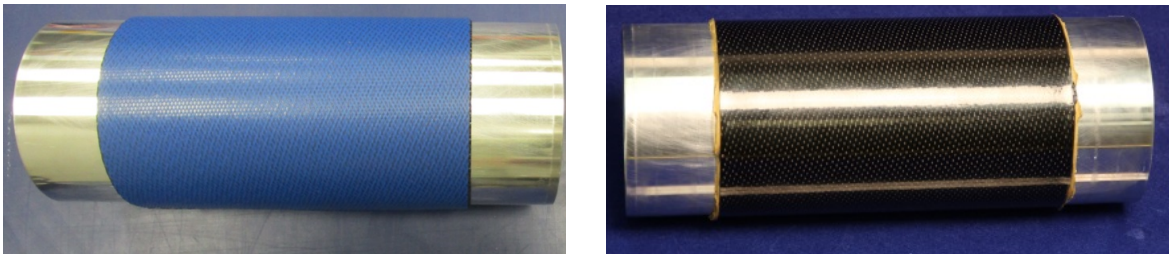

Figure 2.1: The bi-material cylinder pre-cure (left) and post-cure (right).

Post-cure and post-machining thickness measurements were taken at eight points about the circumference for the bi-material cylinder for more accurate modeling and to obtain a distribution to be used in the uncertainty quantification study. Additional details of the measurement process can be found in Section 5.1 and the average thicknesses are given in Table 2.1.

Table 2.1: Average layer thicknesses used in the split ring finite element model.

Model	**Total Thickness (mm)**	**Aluminum (mm)**	**Composite (mm)[1]**
Carbon Fiber (no skew)	3.380	1.883	1.497
Carbon Fiber (45° skew)	3.455	1.908	1.547
Glass Fiber (no skew)	3.341	1.856	1.485

[1]Calculated from the reduction of the total thickness by the thickness of the aluminum layer.

Table 2.2: Stress free scribe line measurements before final machining.

Carbon Fiber (no skew)	**Carbon Fiber (45° skew)**	**Glass Fiber (no skew)**
47.93 mm	49.43 mm	49.45 mm

Prior to the machining operations, scribe lines were etched into the composite (to later position the extensometer) and were measured such that the stress free temperature could be determined (Table 2.2). The bi-material cylinder was then machined on a lathe in order to produce up to six 25.4 mm wide rings, ignoring the excess aluminum and composite of the ends. If the composite was damaged during this process, the bi-material ring was discarded and did not become a split ring. The final machining step removed a 30.48 mm sector from the bi-material ring. A jig was used to prevent spring in due to residual stress that could result in binding the cutting blade. Including the width of the cutting blade, the total width

of removed material was 32.26 mm. Once the bi-material split ring was removed from the jig, it closed in on itself due to the residual stress at the interface between the aluminum and composite. Figure 2.2 displays portions of the machining process and Figure 2.3 shows a final machined bi-material split ring for each of the variants.

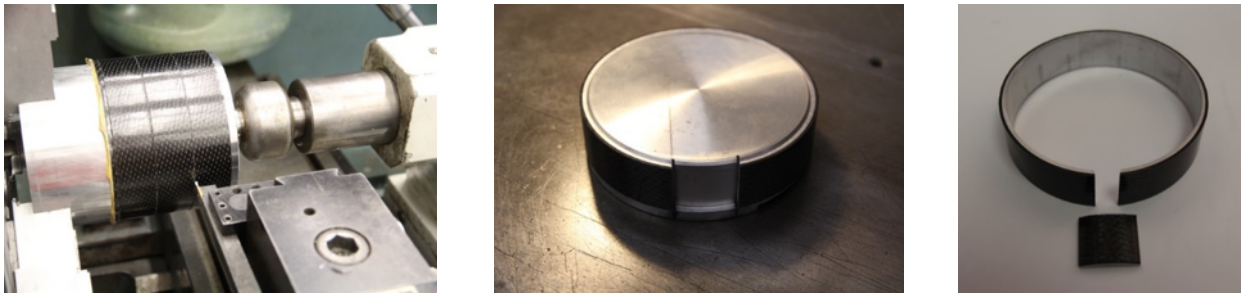

(a) (b) (c)

Figure 2.2: Machining process of the bi-material split ring: (a) lathe cutting cylinder into rings, (b) split ring in jig after sector removal, (c) split ring removed from jig.

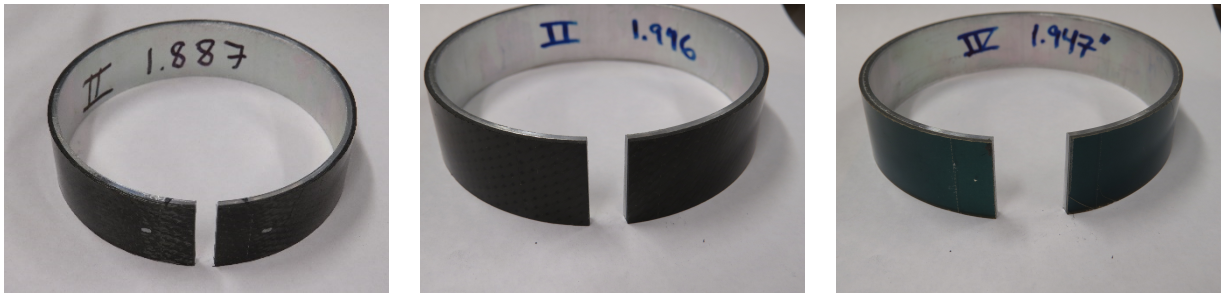

(a) (b) (c)

Figure 2.3: Final bi-material split rings (numbered and with scribe line measurements): (a) carbon fiber (no skew), (b) carbon fiber (45° skew), (c) glass fiber (no skew)

2.2 Procedure

By using a symmetric stack sequence for the composite in both geometries, any thermal residual stress would, in most part, be solely due to the polymer shrinkage and the coefficient of thermal expansion (CTE) mismatch between the aluminum and composite material. The approach in this experimental phase of the investigation is to observe and measure the width of the scribe lines as a function of temperature.

Figure 2.4 shows the experimental setup within the environmental chamber where the scribe lines were measured throughout the heating and cooling process using an extensometer attached to the split ring at the scribe lines. Thermocouples were attached to both the aluminum and composite to monitor the temperatures (not control the environment chamber,

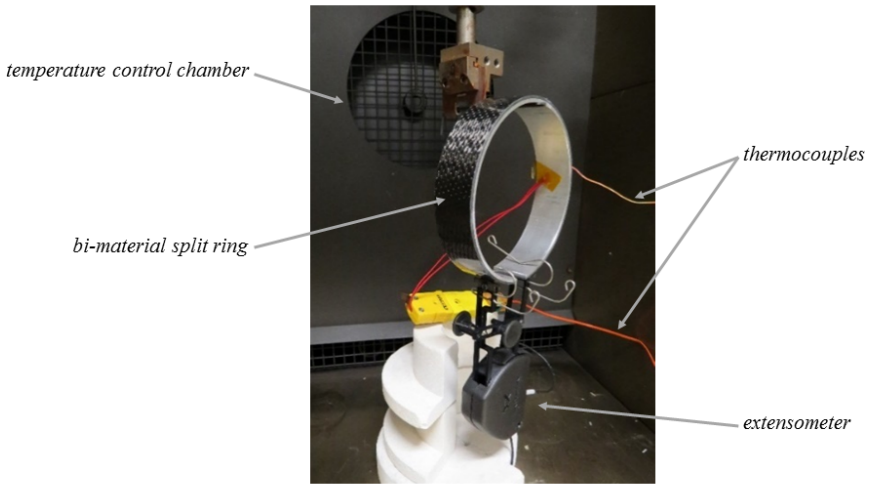

Figure 2.4: Experimental setup.

which used its own sensors). The static loads of the extensometer and of the split ring itself are assumed to have negligible effect on the width of the scribe lines.

The temperature was increased from room temperature (approximately 25°C) to 170°C at a rate of 0.5°C per minute and then decreased back to room temperature at the same rate (Figure 2.5). A faster rate would produce large temperature differences between the aluminum and composite due to their differing thermal properties and would result in a hysteresis loop over the heatup and cooldown cycle. Even with the slow rate to minimize the temperature difference, during the heatup phase, temperature differences between the aluminum and the composite could exceed 5°C, whereas the cooldown minimized the temperature differences to be less than 1°C, as shown in Figure 2.5. This is most likely due to the heater being more active during the heatup (as seen by the greater of number of spikes in the temperature difference). Therefore, the results of the cooldown were used to compare to the simulations.

2.3 Results

The following figures show the distance between scribe lines as recorded by the extensometer for each variant of the bi-material split ring. Two experiments were completed for the carbon fiber (45° skew) and glass fiber (no skew) split rings and only one was completed for the carbon fiber (no skew) split ring.

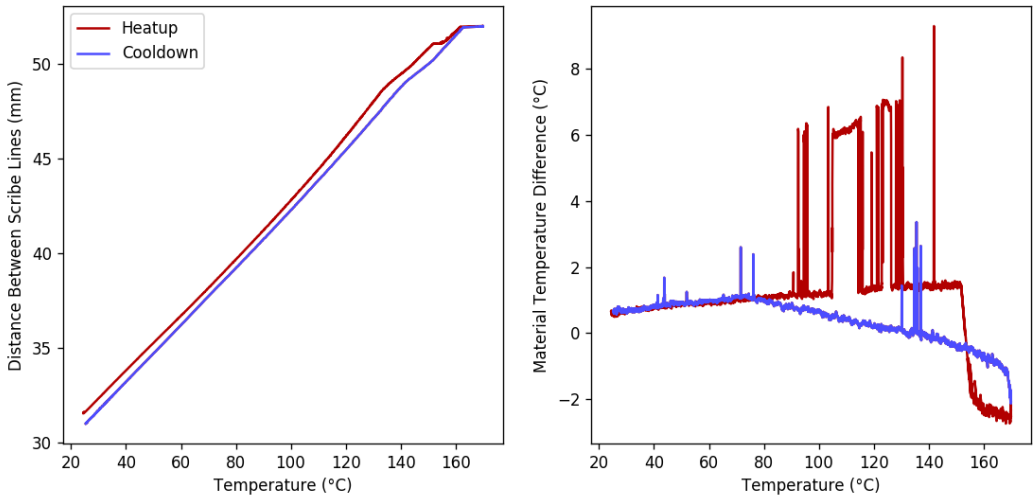

Figure 2.5: Comparison between heatup and cooldown legs of the experiment: distance between scribe lines (left) and aluminum-composite temperature difference (right)

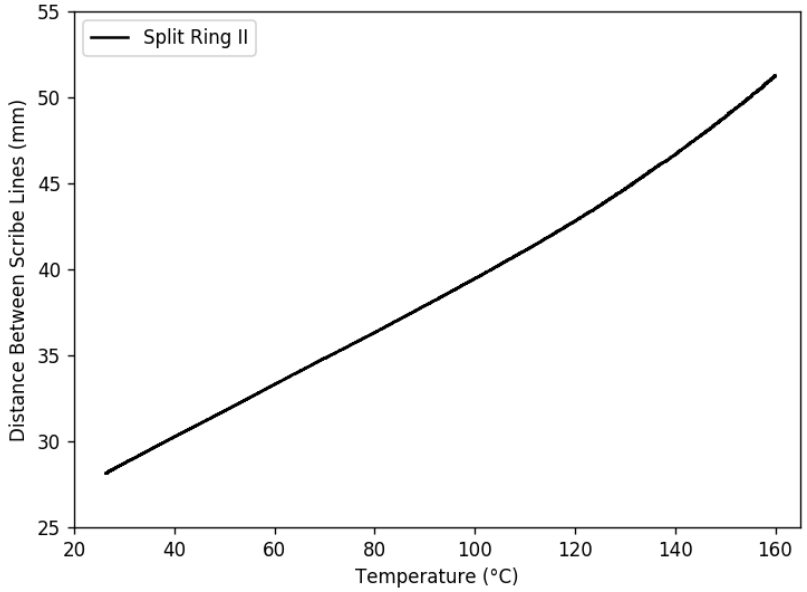

Figure 2.6: Measured distance between scribe lines as a function of temperature, carbon fiber (no skew).

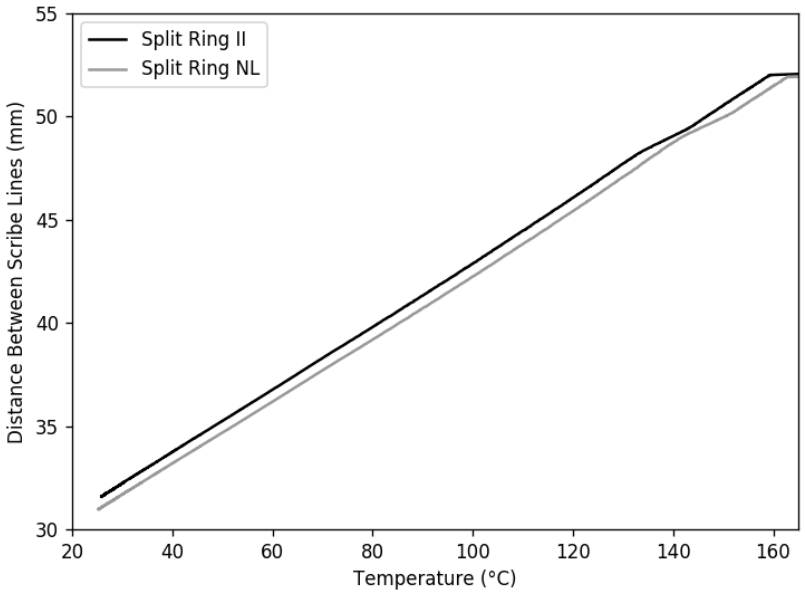

Figure 2.7: Measured distance between scribe lines as a function of temperature, carbon fiber (45° skew).

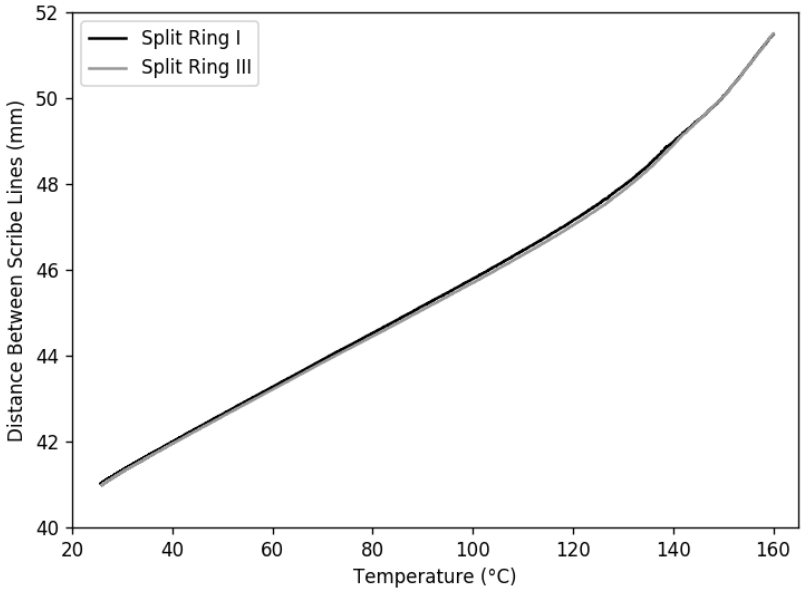

Figure 2.8: Measured distance between scribe lines as a function of temperature, glass fiber (no skew).

2.4 Stress Free Temperature Determination

Defining the stress free temperature (T_{sf}) accurately is the most important property to achieve accurate predictions of the final residual stress state of any bi-material geometry. In the simulation methodology used (Section 3.1), the stress free temperature is not only used to indirectly account for the polymer shrinkage of the composite, but it also sets the temperature difference (ΔT) that, with the CTEs, is used to calculate the thermal strains of each material. Previously, the stress free temperature of an aluminum/carbon fiber composite plate was determined by heating the bi-material plate until it visually returned flat [8]. Relying on visual inspection to determine the stress is not particularity reliable nor accurate.

To achieve greater accuracy, the stress free temperature for each of the split rings was determined by measuring the distance between the scribe lines (at room temperature) prior to removing material to create the split ring (Table 2.2). Then, using the experimental results, the stress free temperature is the temperature at which the scribe lines return to the same distance (Figure 2.9). This methodology is not exact as the state in which the scribe lines was first measured is not stress free (since it was measured post-cure); however, the strains are assumed to be small due to the stiffness of the closed cylinder geometry. Therefore, it is assumed that there is a negligible difference in distance between the scribe lines measured post-cure at room temperature and the true stress free state. Table 2.3 gives the measured stress free temperatures for all experiments.

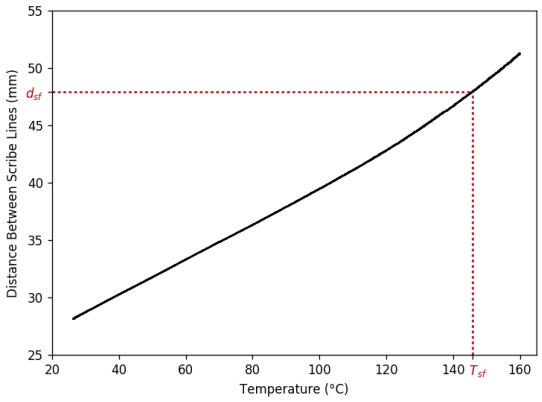

Figure 2.9: Example of stress free temperature calculation - carbon fiber (no skew).

Table 2.3: Stress free temperature values for each experiment.

Experiment	**Carbon Fiber (no skew)**	**Carbon Fiber (45° skew)**	**Glass Fiber (no skew)**
I	145.8	-	145.2
II	-	145.3	144.8
NL	-	143.0	-

Chapter 3

Finite Element Model

The finite element model (FEM) of the split ring was developed to be both computationally efficient and robust in order to support uncertainty quantification studies that require many simulations. The following sections outline the information used to created the split ring FEM and the assumptions that were necessary.

3.1 Simulation Process

The simulation process used to determine the residual stress in the bi-material split rings assumes that all the residual stress is generated by two factors: the polymer shrinkage of the composite's matrix and the coefficient of thermal expansion (CTE) mismatch between the differing materials. The effect of the polymer shrinkage is indirectly accounted for through the calibration to an experimentally determined stress free temperature, where as the CTEs of the materials were explicitly modeled in the material definitions.

During the curing process, the composite's polymer matrix will volumetrically shrink and impart a residual stress in the component. As a bi-material geometry begins to cool, the mismatched coefficients of thermal expansion will eventually nullify the residual stress induced by the polymer shrinkage at the stress free temperature resulting in a stress free temperature that is lower than the cure temperature [9]. Therefore, heating a bi-material geometry to the experimentally determined stress free temperature instead of the cure temperature allows for the effect of polymer shrinkage to be indirectly incorporated (Figure 3.1). Based on this, the simulation reduces the analysis cure cycle to a simple ramp up to the stress free temperature and a ramp back to room temperature.

In total, the simulation consists of three steps with a fourth step to match the thermal cycle of the experiments:

The first step of the simulation isothermally heats the split ring from room temperature to the stress free temperature (144.1°C and 144.7°C for the carbon and glass fiber composite split rings, respectively) where the simulation is then stopped. During this step the composite is uncured and is modeled as a compliant, incompressible material such that it does not constrain the thermal expansion of the aluminum. Stopping the analysis at the stress free temperature allows the cured composite material to be activated at a known stress free state

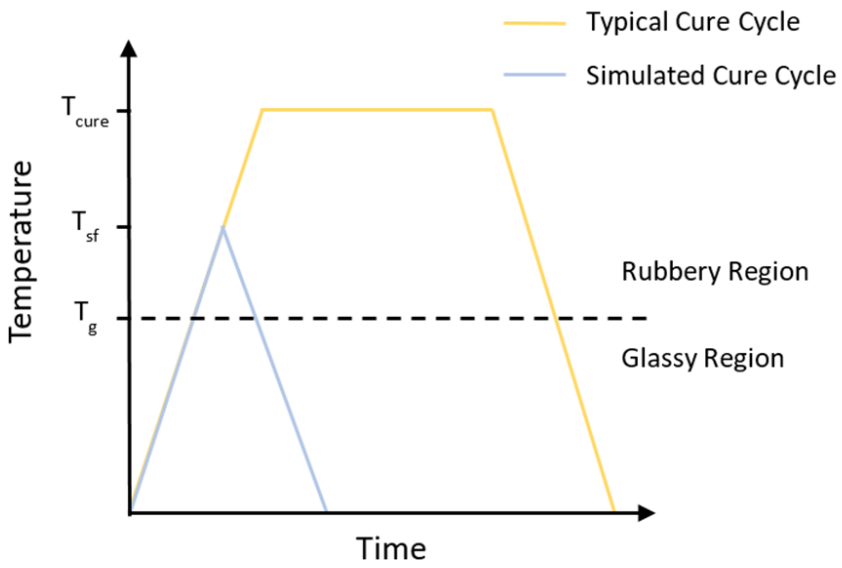

Figure 3.1: Comparison of the temperature history for the simulated cure cycle (Steps 1 and 2) and an actual cure cycle (simplified).

for the next analysis step while the aluminum maintains its size and shape. Furthermore, it allows for the deactivation of the un-cured, compliant material properties and the activation of the cured material properties in the subsequent analysis step. This simplifies the simulation of the curing process by simulating the composite material property transformation as a step change.

The second step performs the deactivation of the un-cured composite materials and the activation of the cured composite materials before cooling the geometries back to room temperature. At the onset of the second step the cured composite and aluminum are activated in a stress free state by only transferring the thermal strains and temperatures from the initial analysis step. As the cylinder begins to cool, residual stresses will begin to develop due to the dissimilar coefficients of thermal expansion.

The residual stresses remain visibly undetectable until the third analysis step where the sector is removed from the cylinder to create a split ring, after which spring-in occurs. The third analysis step simply solves for static equilibrium of the new state.

3.2 Analysis Software

All simulations used Sandia National Laboratories' Sierra/SolidMechanics code, Adagio [10]. Adagio is a Lagrangian, three-dimensional implicit code for the finite element analysis of

solid, quasi-static structures, which is suitable for simulating the bi-material split rings. Adagio makes use of a multi-level solver, of which the solution core is a nonlinear, conjugate gradient algorithm that can iteratively find a solution that is within some user-defined tolerance of equilibrium. Use of the multi-level solver within Adagio aids in the solution of problems containing such challenging aspects as contact, materials with non-linear responses or extreme differences in stiffness, and material failure with element death.

Adagio can make use of a nodal or full tangent preconditioner to improve the condition number of the stiffness matrix for the conjugate gradient solver. The nodal preconditioner only provides the diagonal terms of the stiffness, which only accounts for the stiffness at each node (i.e. there is no coupling between nodes). The full tangent preconditioner, as its name states, accounts for the full stiffness matrix. The nodal preconditioner is much more efficient, but the full tangent preconditioner is more effective with poorly conditioned problems, such as the bending response of long, slender members. The conjugate gradient solver has difficulty solving for equilibrium in the third simulation step where a portion of the bi-material ring is removed. Convergence has been achieved with the use of a combination of both preconditioners, where the problem begins with the nodal preconditioner before switching to the full tangent preconditioner with the `minimum smoothing iterations` command. However, the full tangent preconditioner is sensitive to the state at which it begins (i.e. the number of iterations using the nodal preconditioner). As a result, to improve robustness of the simulation, the third simulation step looped through an increasing number of nodal preconditioner iterations until a converged solution was found.

3.3 Element Formulation

The bi-material split ring models were simulated with eight-noded hexahedral elements. For ease of application and decreased computational time, the uniform gradient element formulation was used (default in Adagio). This formulation conducts the volume integration with single point Gaussian quadrature and, although it is computationally efficient, it has the noteworthy disadvantage of zero energy, or hourglassing, modes. However, a simple method of controlling this undesirable behavior is the application of a small elastic stiffness that is capable of stopping the formation of any anomalous modes without affecting the global response. Sierra Adagio is automatically equipped with a default hourglassing stiffness of 0.05 and this value was used in all of the completed analyses. In addition to the default added stiffness, an hourglassing viscosity of 0.03 was also added to the simulations. Within Adagio, small artificial viscosities can be specified for models exhibiting hourglass modes to inhibit opposing rotations within the mesh.

3.4 Model Geometry and Boundary Conditions

The geometry for each split ring variant was generated and meshed in three-dimensions using Cubit. For simplicity, the composite layer of the split ring was modeled as a single, homogeneous layer (ignoring the individual plies). This prevents the mesh from becoming extremely large and computationally expensive to run.

The geometry of the split rings was specified as a combination of both nominal and measured dimensions. The inner diameter of the aluminum pipe was assumed to be the nominal inner diameter of the number 4, schedule 10 pipe: 4.26 inches, or 108.2 mm. The thickness of the aluminum and composites were measured for better model accuracy with respect to the manufactured part. The aluminum and composite were modeled with uniform thickness (based on the average of eight measurements), as the small dimensional variances in the thicknesses are assumed to be negligible with regards to the final residual stress state of the split ring. Since the composite thickness could not be directly measured, the geometry was defined by the aluminum thickness and total thickness. Additional details of the measurement process can be found in Section 5.1 and the average thicknesses are given in Table 2.1.

Although the split ring was machined from a larger cylinder, the aluminum is expected to remain elastic and, therefore, modeling the split ring at its final width of 25.4 mm is acceptable. For computational efficiency, the split ring was modeled in quarter symmetry with 180°and half the total width (12.7 mm). Symmetry was specified on the xy and yz planes and a single node along the cut surface was held at zero y-displacement to prevent any motion (Figure 3.3). The geometry incorporated partitions for the removed portion of the split ring, the material eliminated by the cutting blade, and the scribe line for comparison to the experiments (Figure 3.2). The cut partition is positioned to create a removed sector with a width of 30.48 mm, which results in a total of 32.26 mm of material removed from the ring (including the width of the cutting blade). Instead of having the simulation eliminate the entire removed sector to create a split ring, just the cut partition was removed because Sierra will fail if all the elements on a processor are eliminated (whether through omit block or element death). Omitting only the cut partition allowed for a greater number of processors to be used and decreased the run time of the refined meshes.

The composite material of the split ring was orientated in cylindrical coordinates. For the glass and carbon fiber composites with no skew, the 11 direction is aligned with the circumference, the 22 direction is aligned parallel with the axis of the split ring, and the 33 direction is radial (normal to the plies). The carbon fiber composite split ring with 45° skew in the fiber orientation simply rotates the material directions of the no skew case by 45° about the 33 direction, as shown in Figure 3.4.

Composites with any ply skew should not be modeled in symmetry as the material directions would become disjoint at the symmetry planes. Furthermore, ply skew will cause the split ring to take a more helical shape, which symmetry planes will prevent. However, in the case of the carbon fiber composite with a skew of 45°, the material properties of the 11 and 22 directions are similar. Therefore, the split ring does not result in helical shape and quarter

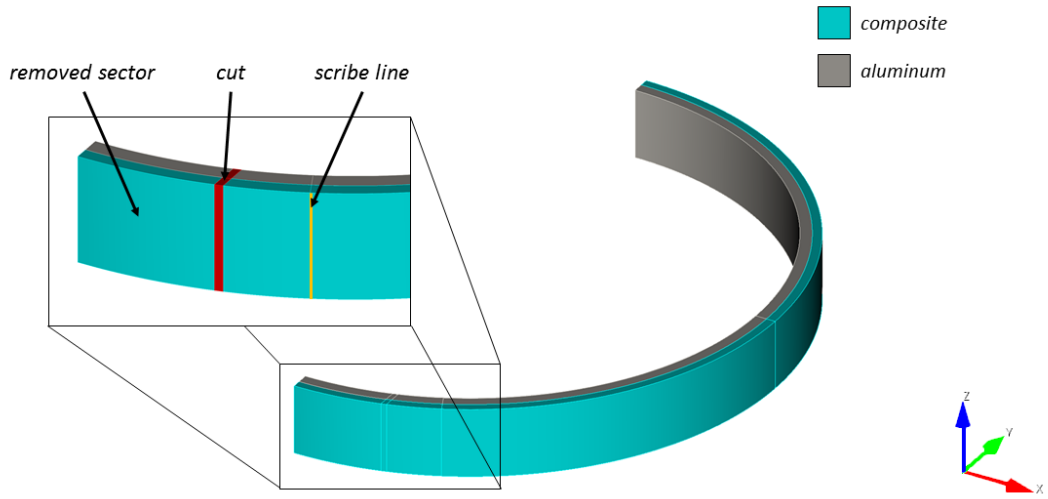

Figure 3.2: Split ring finite element model geometry.

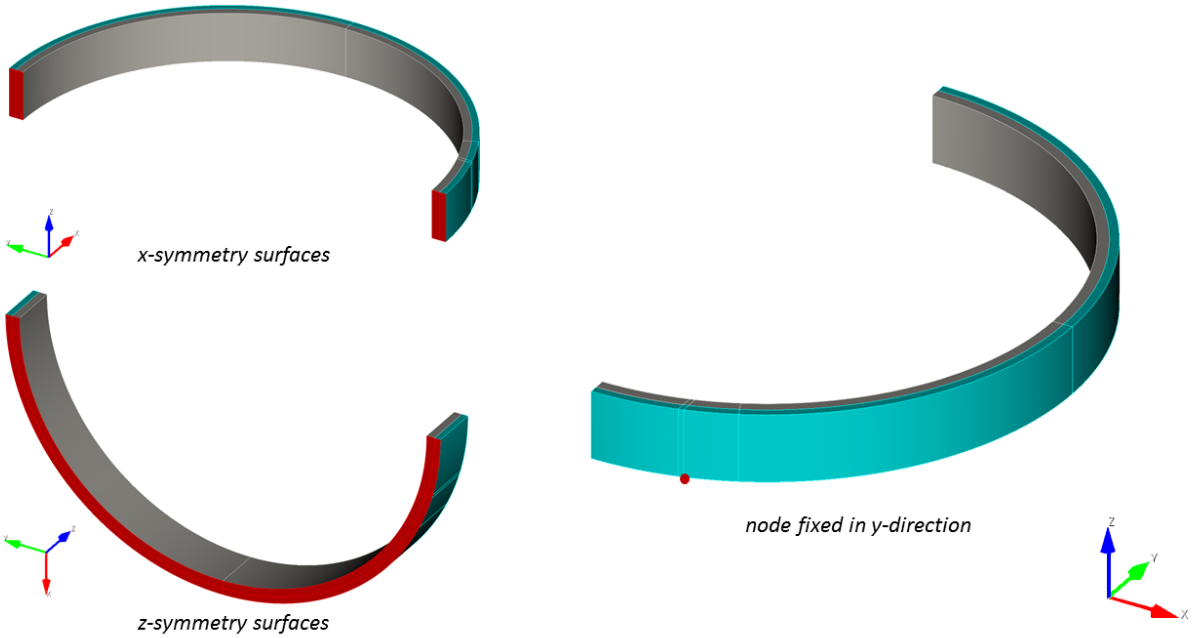

Figure 3.3: Boundary conditions for the split ring finite element model.

symmetry is an acceptable assumption.

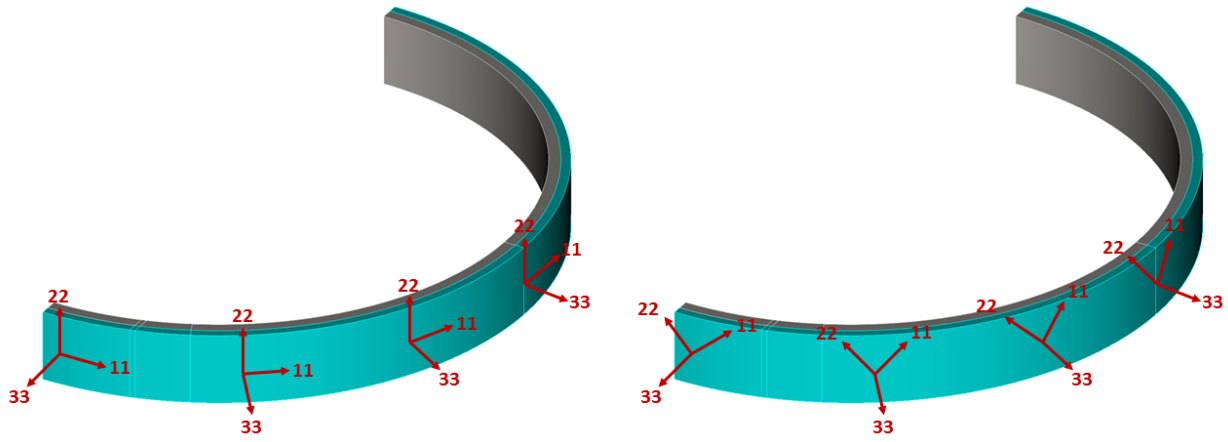

Figure 3.4: Composite material orientations for the split ring finite element model: No skew (left) and 45° skew (right).

3.5 Material Models

The specification of three materials is needed to simulate the curing process of the bi-material split ring: aluminum, un-cured composite, and cured composite. Additionally, each material model was specified as temperature independent or temperature dependent, where the elastic properties and coefficients of thermal expansion were specified as functions of temperature. The temperature independent models assumed properties at 25°C.

3.5.1 Aluminum Mechanical Properties Specificaiton

The aluminum was modeled using Adagios elastic material model for temperature independent properties and the thermoelastic material model for the temperature dependent properties. Both models produce linear elastic behavior and require the specification of the density, Youngs Modulus, and Poissons ratio [10]. The thermoelastic model allows the Youngs Modulus and Poissons ratio to be specified as functions (of temperature), whereas they must be constant in the elastic model. These models are sufficient as no yielding or failure is expected in to occur in the aluminum, nor has it occurred in previous experiments [8, 11].

A temperature dependent Youngs modulus for aluminum is given by Table TM-2 of the ASME Boiler and Pressure Vessel Code (BPVC), as shown in Table 3.1 [12].

Table 3.1: Aluminum mechanical properties at various temperatures for an elastic material model.

Temperature (°C)	**-75**	**25**[2]	**100**	**150**	**200**
Density (kg/m^3)[1,3]	2,700	2,700	2,700	2,700	2,700
E (GPa)	72.0	69.0	66.0	63.0	60.0
ν[1]	0.33	0.33	0.33	0.33	0.33

[1]Temperature dependent values were not given by Table PRD of the ASME BVPC.
[2]Temperature at which the properties for temperature independent model were defined.
[2]Sierra Adagio requires the specification of density for all material models. For implicit quasi-static analyses, the density is arbitrary and a constant value has no affect on the solution.

3.5.2 Un-Cured Composite Mechanical Properties Specification

The uncured composite was modeled using homogenized material properties and Sierra Adagio's elastic orthotropic material model (elastic_orthotropic) [10]. The elastic orthotropic material model calls for the density and the regular nine independent constants (Youngs modulus, shear modulus, and Poissons ratios in the three material directions) to be fully defined. The material model then uses coordinate rotations to properly align the material coordinate system.

In its un-cured state, the epoxy matrix of the composite materials has the ability to flow and will not restrict the thermal expansion of the aluminum. As such, the un-cured composite was modeled as a compliant, incompressible, and isotropic elastic material using Sierra Adagios elastic orthotropic model. Using the elastic orthotropic model instead of a basic elastic model was necessary to ensure the proper fields were present within the model such that restarting the simulation with the cured composite material properties was successful. However, a perfectly compliant and incompressible material (E=0 Pa and =0.5) resulted in non-convergence. This was resolved by using properties sufficiently similar, as shown in Table 3.2.

Furthermore, the un-cured composite was given the same coefficient of thermal expansion (CTE) as the aluminum in the in-plane material directions to prevent any restriction of the aluminum due to differences in thermal strains (SEE SECTION X and X). The cured composite CTE was specified for the material direction normal to the plies (out-of-plane or the 33 direction) in order to maintain zero thermal strain at room temperature. This ensured that the thickness of the composite was retained as the thickness was specified in the mesh as the final, cured thickness.

The mechanical properties of the un-cured composite remain constant for both the temperature dependent and independent models with the temperature dependent only differing from the temperature independent model by the use of aluminums temperature dependent thermal strains.

Table 3.2: Un-Cured composite mechanical properties.

Density (kg/m^3)	Young's Modulus (MPa)	Poisson's Ratio
1,600	1	0.4999

3.5.3 Cured Composite Mechanical Properties Specification

Sierra Adagio's elastic orthotropic material model was also used for modeling the cured composite with homogenized material properties. A temperature dependent and temperature independent material model was specified for both the carbon and glass fiber composites (the temperature independent model assumed room temperature, 25°C, mechanical properties).

The mechanical properties of the cured composite materials were determined through experiments for E_{11}, $E_{22,}$ ν_{12}, and G_{12} at 54°C, 25°C, and 71°C. The remaining mechanical properties were determined through other experiments at room temperature (25°C) or through micromechanical modeling and then given temperature dependence by scaling the temperature dependence of G_{12}. For temperatures above 71°C, the temperature dependence was extrapolated. Table 3.3 and Table 3.4 give the mechanical properties of the carbon and glass fiber composites, respectively.

For the carbon fiber composite, the mechanical properties dominated by the fibers (E_{11}, E_{22}, and ν_{12}) showed little or no temperature dependence and were held constant at their room temperature values. The values for ν_{13} and ν_{23} were also held constant for both composites.

Table 3.3: Carbon fiber composite mechanical properties at various temperatures for an elastic orthotropic material model.

Temperature (°C)	**-54**	**25**	**71**	**160**
Density (kg/m^3)[1]	1,600	1,600	1,600	1,600
E_{11} (GPa)	63.86	63.86	63.86	63.86
E_{22} (GPa)	62.74	62.74	62.74	62.74
E_{33} (GPa)	12.17	8.59	6.50	2.46
ν_{12}	0.048	0.048	0.048	0.048
ν_{13}	0.408	0.408	0.408	0.408
ν_{23}	0.408	0.408	0.408	0.408
G_{12} (GPa)	4.87	3.44	2.60	0.99
G_{13} (GPa)	4.63	3.27	2.47	0.94
G_{23} (GPa)	4.61	3.25	2.46	0.93

[1]Sierra Adagio requires the specification of density for all material models. For implicit quasistatic analyses, the density is arbitrary and a constant value has no affect on the solution.

Table 3.4: Glass fiber composite mechanical properties at various temperatures for an elastic orthotropic material model.

Temperature (°C)	**-54**	**25**	**71**	**160**
Density (kg/m^3)[1]	1,600	1,600	1,600	1,600
E_{11} (GPa)	28.55	24.75	22.54	18.27
E_{22} (GPa)	26.54	23.10	21.09	17.21
E_{33} (GPa)	14.56	9.72	6.91	1.46
ν_{12}	0.152	0.130	0.117	0.092
ν_{13}	0.36	0.36	0.36	0.36
ν_{23}	0.36	0.36	0.36	0.36
G_{12} (GPa)	5.16	3.48	2.45	0.52
G_{13} (GPa)	4.40	2.94	2.09	0.44
G_{23} (GPa)	4.40	2.94	2.09	0.44

[1]Sierra Adagio requires the specification of density for all material models. For implicit quasistatic analyses, the density is arbitrary and a constant value has no affect on the solution.

3.5.4 Temperature Dependent Coefficient of Thermal Expansion Specification

The coefficients of thermal expansion (CTEs) were defined as a function of temperature and then converted to thermal strains for use within the Sierra material property definition. For the case of the elastic orthotropic materials, a CTE for each of the three directions was specified.

Temperature dependent CTEs for aluminum were found in Table TE-2 of the ASME BPVC [12]. The table gives average CTE for the temperature ranges 20°C to 100°C (23.4e-06 K^{-1})and 20°C to 200°C (24.5e-06 K^{-1}) [12]. Using these CTEs, thermal strains were calculated at 100°C and 200°C and applied as a piecewise linear function in Adagio (Table 3.5).

The CTEs were measured for each of the three material directions from -50°C to 150 °C in increments of 10°C for the composite materials. Since the experimental temperature range did not drop below 20°C, temperature below were not considered (except when calculating the average CTE of the composites glassy region). Table 3.6 and 3.8 give the average temperature dependent CTEs for carbon and glass fiber, respectively. The thermal strains for the composite materials (Table 3.7 and 3.9) were calculated through numerical integration of the CTEs using a midpoint rule Reimann sum:

$$S = \sum_{T_i}^{T_f} \left[\frac{CTE_i + CTE_{i-1}}{2} \right] * \Delta T \tag{3.1}$$

where T_i is the reference temperature having a thermal strain of zero (20°C), T_f is the final evaluated temperature, and ΔT is the step change in temperature (10°C).

The Reimann sum was calculated at all temperatures (other than the reference temperature) and offers an adequate approximation of the thermal strains to provide Adagio with a piecewise linear function.

Table 3.5: Aluminum temperature dependent thermal strain specification (1.0e-04 mm/mm).

Temperature (°C)	**20**	**100**	**200**
Isotropic `th_str`	0.0	18.72	44.10

Table 3.6: Carbon fiber composite temperature dependent CTEs (1.0e-06 K^{-1}).

Temperature (°C)	**20**	**30**	**40**	**50**	**60**	**70**	**80**	**90**	**100**	**110**	**120**	**130**	**140**	**150**
11 Direction	2.9	2.8	2.9	3.2	3.4	3.6	3.9	4.1	3.9	3.6	1.9	1.0	1.0	2.0
22 Direction	3.2	3.3	3.3	3.6	3.7	3.9	4.0	4.2	4.4	4.4	3.3	2.8	2.1	2.2
33 Direction	55.6	57.4	61.3	64.2	68.9	7.7	79.2	87.0	100.3	130.0	190.1	226.6	227.6	231.3

Table 3.7: Carbon fiber composite temperature dependent thermal strain (1.0e-04 mm/mm).

Temperature (°C)	**20**	**30**	**40**	**50**	**60**	**70**	**80**	**90**	**100**	**110**	**120**	**130**	**140**	**150**
11 Direction	0.0	0.29	5.74	0.88	1.20	1.55	1.93	2.32	2.72	3.10	3.37	3.52	3.61	3.76
22 Direction	0.0	0.32	0.65	1.00	1.36	1.74	2.13	2.54	2.97	3.41	3.80	4.11	4.36	4.58
33 Direction	0.0	5.65	11.6	17.9	24.5	31.6	39.3	47.6	57.0	68.5	84.5	105.3	128.0	151.0

Table 3.8: Glass fiber composite temperature dependent CTEs (1.0e-06 K^{-1}).

Temperature (°C)	**20**	**30**	**40**	**50**	**60**	**70**	**80**	**90**	**100**	**110**	**120**	**130**	**140**	**150**
11 Direction	13.5	14.1	14.5	14.7	15.6	15.7	16.2	16.4	16.6	16.0	13.6	10.7	10.6	10.3
22 Direction	13.9	14.3	14.6	15.5	15.7	16.0	17.0	17.3	17.8	18.0	17.2	14.6	11.9	10.2
33 Direction	46.3	48.5	51.8	55.6	59.3	64.0	69.8	78.8	94.3	128.7	184.9	241.6	255.5	262.8

Table 3.9: Glass fiber composite temperature dependent thermal strain (1.0e-04 mm/mm).

Temperature (°C)	**20**	**30**	**40**	**50**	**60**	**70**	**80**	**90**	**100**	**110**	**120**	**130**	**140**	**150**
11 Direction	0.0	1.38	2.81	4.27	5.79	7.35	8.94	10.6	12.2	13.9	15.3	16.6	17.6	18.7
22 Direction	0.0	1.41	2.85	4.36	5.92	7.51	9.16	10.9	12.6	14.4	16.2	17.8	19.1	20.2
33 Direction	0.0	4.74	9.76	15.1	20.9	27.0	33.7	41.2	49.8	61.0	76.6	98.0	122.8	148.7

3.5.5 Temperature Independent Coefficient of Thermal Expansion Specification

The temperature independent material models were given an average values for the CTE: the aluminum was given a single value for the experimental temperature range, whereas the composites were given two - one below and one above the glass transition temperature.

The CTE used for the aluminum was the average CTE between 20°C and 100°C (23.4e-06 K^{-1}). This CTE covers the majority of the experimental temperature range and is not influenced by data outside the experimental temperature range (e.g. the average CTE from 20°C to 200°C).

Two CTEs were used in the composites to account for the difference in CTEs between the glassy and rubbery regions of the composite. While this is not strictly temperature independent, this allows the simulation to capture the two distinct material property realms of the composite, which is evident in the experiments where the slope changes at the glass transition temperature. The temperature independent CTEs were determined by averaging the temperature dependent CTEs above and below T_g (in some cases outliers were ignored). Table 3.11 and 3.13 give the temperature independent CTEs for both the carbon and glass fiber composites, respectively. The corresponding thermal stains are given in Tables 3.12 and 3.14. Figures 3.5 through 3.10 show a comparison of the two sets of CTEs and the resulting thermal strains.

Table 3.10: Aluminum temperature independent thermal strain specification (1.0e-04 mm/mm).

Temperature (°C)	**20**	**100**	**200**
Isotropic `th_str`	0.0	18.72	42.12

Table 3.11: Carbon fiber composite temperature independent (average) CTEs (1.0e-06 K^{-1})

Temperature (°C)	$< T_g^1$	$> T_g$
11 Direction	3.15	0.95
22 Direction	3.62	2.18
33 Direction	63.7	228.5

[1]Average CTEs below T_g were averaged over all temperatures sampled in the glass region (-50°C to T_g).

Table 3.12: Carbon fiber composite temperature independent thermal strain specification (1.0e-04 mm/mm)

Temperature (°C)	**0**	T_g	**150**
11 Direction	0.0	3.31	3.55
22 Direction	0.0	3.81	4.35
33 Direction	0.0	67.0	123.8

Table 3.13: Glass fiber composite temperature independent (average) CTEs (1.0e-06 K^{-1})

Temperature (°C)	$< T_g^1$	$> T_g$
11 Direction	14.32	11.30
22 Direction	14.95	13.50
33 Direction	58.9	236.2

[1]Average CTEs below T_g were averaged over all temperatures sampled in the glass region (-50°C to T_g).

Table 3.14: Glass fiber composite temperature independent thermal strain specification (1.0e-04 mm/mm)

Temperature (°C)	**0**	T_g	**150**
11 Direction	0.0	12.9	17.4
22 Direction	0.0	13.4	18.9
33 Direction	0.0	52.9	148.0

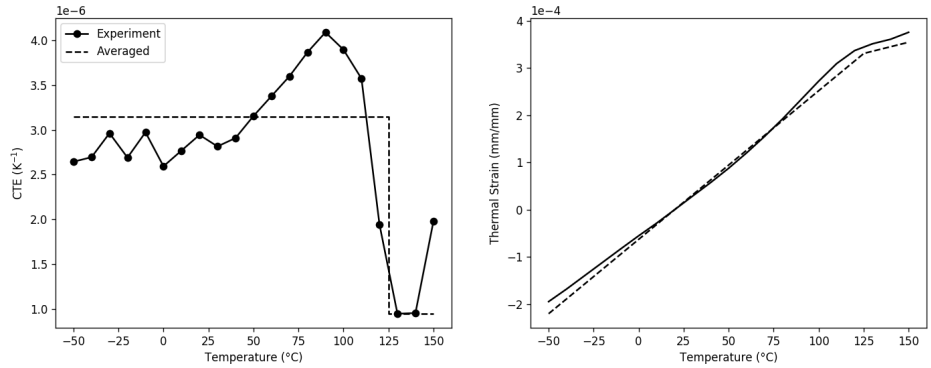

Figure 3.5: Carbon fiber composite temperature dependent and averaged 11 direction CTE comparison.

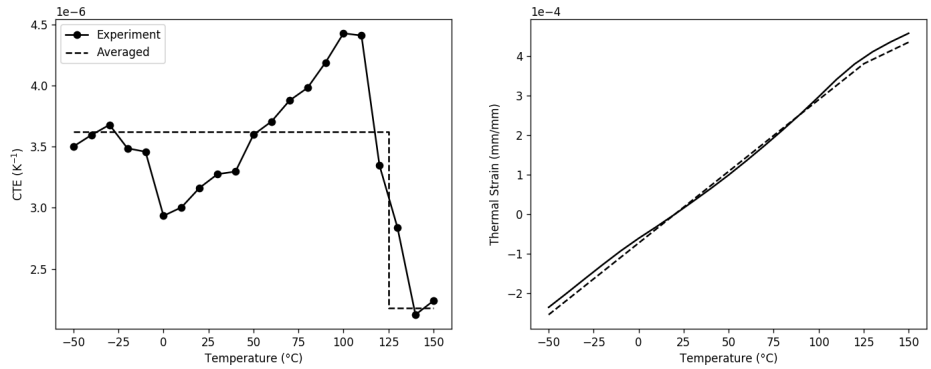

Figure 3.6: Carbon fiber composite temperature dependent and averaged 22 direction CTE comparison.

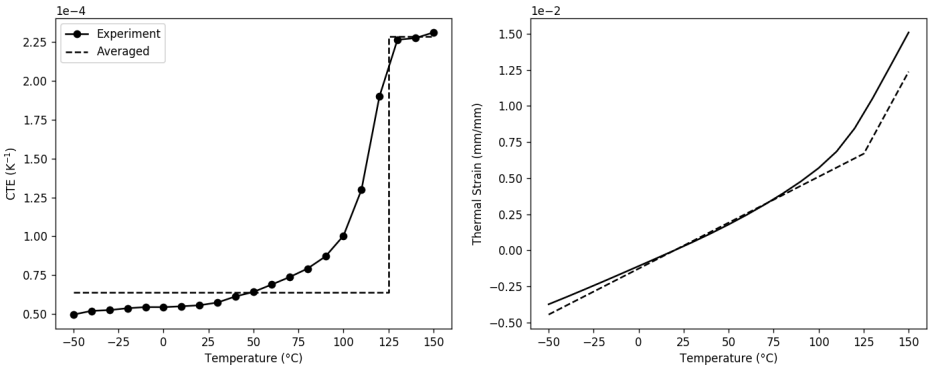

Figure 3.7: Carbon fiber composite temperature dependent and averaged 33 direction CTE comparison.

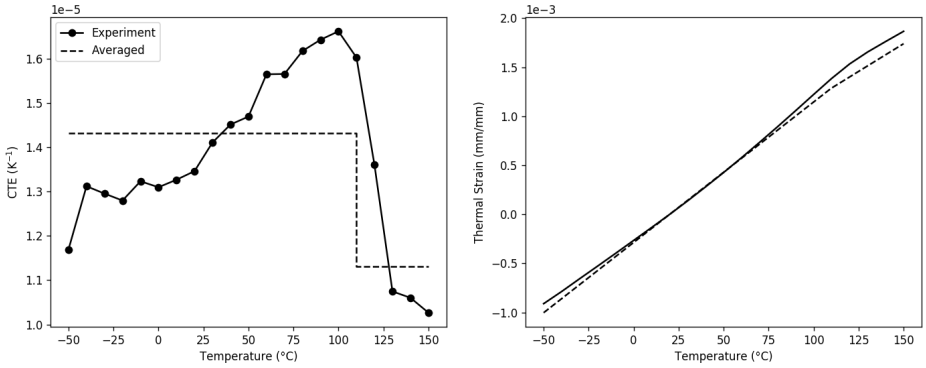

Figure 3.8: Glass fiber composite temperature dependent and averaged 11 direction CTE comparison.

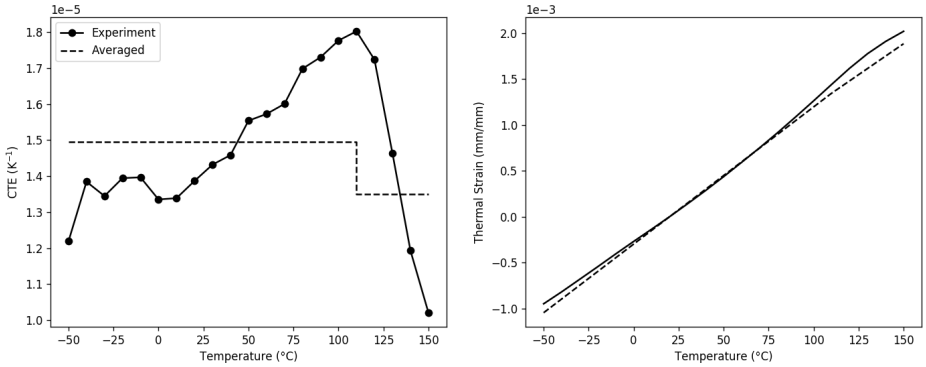

Figure 3.9: Glass fiber composite temperature dependent and averaged 22 direction CTE comparison.

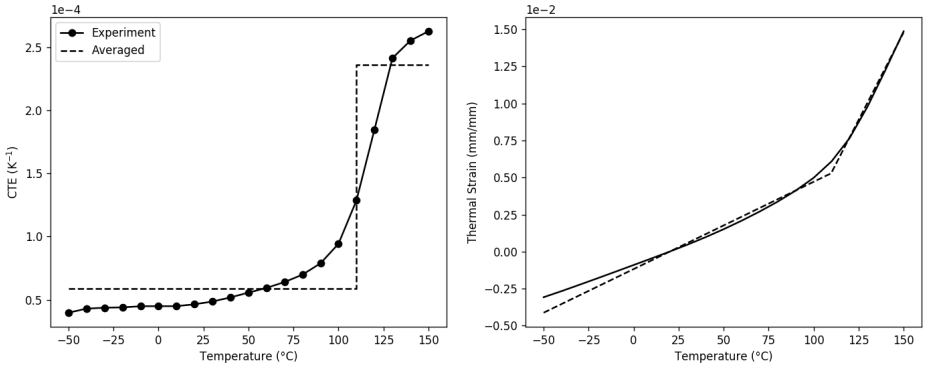

Figure 3.10: Glass fiber composite temperature dependent and averaged 33 direction CTE comparison.

Chapter 4

Nominal Simulation

As discussed in Section 3.5, both temperature dependent and independent material models were defined for the aluminum and composites. Before proceeding to the sensitivity and uncertainty quantification studies, a down select of sorts was necessary to reduce the number of studies, and therefore the computational cost, by selecting only one material model. The methods described in the previous chapter were used with the nominal material properties provided in Section 3.5 to complete a preliminary validation of the bi-material split rings. The results preliminary validation presented in this chapter compares the performance of the temperature dependent and independent material models with respect to the experimental results from Section 2.3.

4.1 Mesh Convergence Study

Before comparing the predicted residual stresses from the finite element simulations with the experimental results, confidence in the simulation's discretization must be demonstrated through a mesh convergence study. Meshing the bi-material split ring to achieve the lowest possible error is desirable; however this requires refined meshes that are computationally expensive. Therefore, the mesh convergence study is used to determine the maximum element size that results in an acceptable level of error, which is important for both the accuracy and efficiency of uncertainty quantification studies. To calculate the discretization error, the continuum (i.e. mesh size equal to zero) value can be estimated using Richardson's extrapolation.

4.1.1 Richardson's Extrapolation

Richardson's extrapolation is an error error estimation technique that allows for the approximation of a higher order estimate of a continuum solution given a series of lower order, discrete solutions [13]. To begin, a discrete solution, f_k can be considered to be the exact solution with the addition of error terms:

$$f_k = f_{exact} + g_1 h_k + g_2 h_k^2 + g_3 h_k^3 + ... \tag{4.1}$$

Where g_i represents the i-th term error coefficient (which are defined in the continuum and are independent of the discretization) and h_k represents a measure of the grid spacing (element size). If a second order method is assumed, $g_1 = 0$, and if solutions for two different meshes exist, the exact solution can be written as:

$$f_{exact} = f_1 + \frac{f_1 - f_2}{r^2 - 1} + H.O.T. \tag{4.2}$$

Where f_1 is solution from the refined mesh and r is the ratio of element sizes (h_2/h_1). Dropping the higher order terms, Equation 4.2 can be generalized for any p-th order method:

$$f_{exact} \approx f_1 + \frac{f_1 - f_2}{r^p - 1} \tag{4.3}$$

In Equation 4.3, p is the order of convergence, or the order of accuracy, and it is related to the behavior of the solution's error. Given at least three solutions corresponding to three different mesh sizes, the value of p can be estimated through the solution of Equation 4.4, in which r is again the ratio of discrete solution mesh sizes and ϵ_{ij} represents the differences in the discrete solutions, or $f_i - f_j$.

$$\frac{\varepsilon_{23}}{r_{23}^p - 1} = r_{12}^p \left(\frac{\varepsilon_{12}}{r_{12}^p - 1} \right) \tag{4.4}$$

4.1.2 Mesh Convergence Results

For each of the bi-material split ring variants, a discrete solution that represented the residual stress state (distance between scribe lines at room temperature) was found at three different levels of mesh refinement. The initial mesh began with one element through the thickness of each material layer and was uniformly doubled for each subsequent refinement, resulting in four elements through the layer thickness for the most refined mesh (Figure 4.1). The mesh of the split rings uses the thickness of the composite layer to set the element size in order to maintain an aspect ratio close to 1:1:1 within the composite layer. This is done to improve computational efficiency of the model and to prevent unrealistic solutions due to poor element quality. Therefore, a mesh convergence study using Richardson's extrapolation for all three split ring variants was conducted. Tables 4.1 through 4.3 show the results of the mesh convergence study along with the respective computational cost for each mesh refinement level and Figures 4.2 through 4.4 show the error convergence rate for each of the split rings. The most refined mesh resulted in mesh discretization errors of 1% or less with reasonable run times below five minutes without requiring more than one compute node; therefore, the most refined mesh was used in all subsequent simulations and studies.

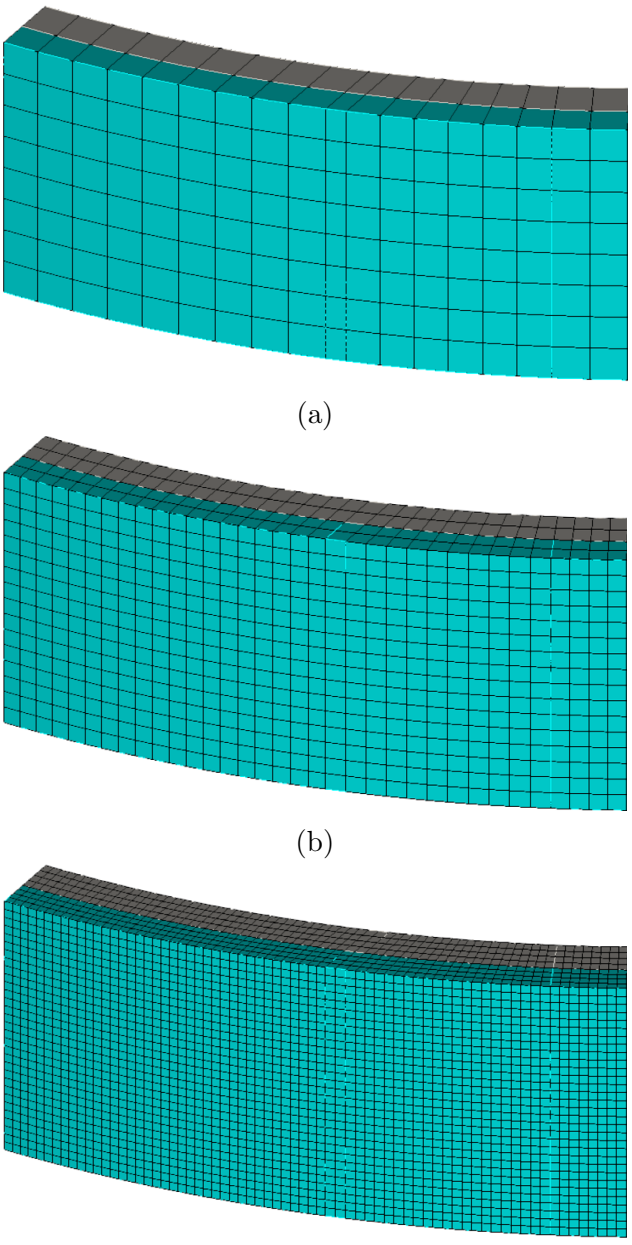

Figure 4.1: Mesh refinement levels: (a) Mesh 3: one through the thickness, (b) 2: two, and (c) 1: four.

Table 4.1: Mesh convergence results for the carbon fiber composite (no skew) split ring.

Mesh	Element Size (mm)	Total Elements (mm)	Distance (mm)	Error	Run Time[1]
3	1.63	1,744	17.20	22.9%	2:20
2	0.81	13,824	21.28	4.6%	1:58
1	0.41	107,136	22.10	0.9%	3:59
Exact	-	-	22.30	-	-

[1]All simulations were run on serrano. Mesh 3 used 1 cpu, 2 used 4, and 1 used 36.

Table 4.2: Mesh convergence results for the carbon fiber composite (45° skew) split ring.

Mesh	Element Size (mm)	Total Elements (mm)	Distance (mm)	Error	Run Time[1]
3	1.63	1,744	21.86	24.5%	1:14
2	0.81	13,824	27.50	5.1%	3:03
1	0.41	107,136	28.67	1.1%	4:47
Exact	-	-	28.97	-	-

[1]All simulations were run on serrano. Mesh 3 used 1 cpu, 2 used 4, and 1 used 36.

Table 4.3: Mesh convergence results for the glass fiber composite (no skew) split ring.

Mesh	Element Size (mm)	Total Elements (mm)	Distance (mm)	Error	Run Time[1]
3	1.51	2,196	37.63	8.4%	1:06
2	0.76	16,320	40.44	1.5%	3:05
1	0.38	133,840	40.95	0.3%	3:52
Exact	-	-	41.07	-	-

[1]All simulations were run on serrano. Mesh 3 used 1 cpu, 2 used 4, and 1 used 36.

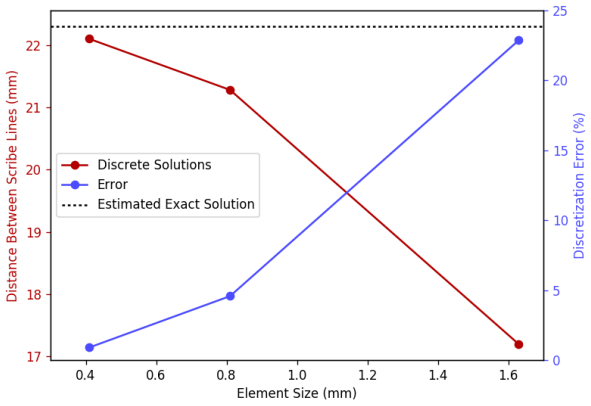

Figure 4.2: Carbon fiber composite (no skew) discrete solutions compared to the estimated continuum value from Richardson's extrapolation.

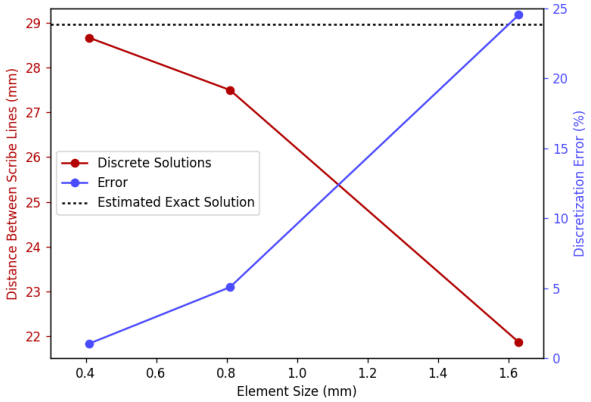

Figure 4.3: Carbon fiber composite (45° skew) discrete solutions compared to the estimated continuum value from Richardson's extrapolation.

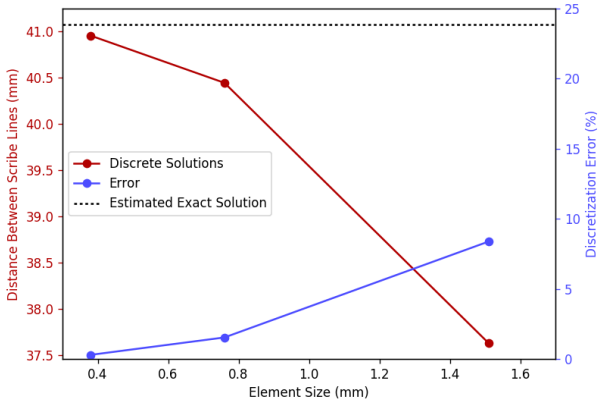

Figure 4.4: Glass fiber composite (no skew) discrete solutions compared to the estimated continuum value from Richardson's extrapolation.

4.2 Results

Using the mesh determined from the mesh convergence study, the simulated bi-material split rings using temperature dependent and independent material models were compared to the corresponding experiment (Figure 4.5 through 4.7).

The plots show that the simulated bi-material split ring residual stress state (as measured by the distance between the scribe lines) agrees reasonably well for both material models. The composites with no skew in their ply orientation appear to be converging with the experimental results as the temperature approaches room temperature, whereas the carbon fiber composite with the 45° skewed plies behaves the opposite. Furthermore, the slopes of the non-skewed composites match more closely with the experiments in both the glassy and rubbery regions of the composite. The split ring with the skewed composite, on the other hand, shows reasonable agreement with the slope in the glass region, but not in the rubbery region. This can be attributed to the fact that the stiffness about the circumference for the composites with no skew is dominated by the fibers (as they are aligned), which do not see a significant change in stiffness over the examined temperature range. However, the carbon fiber skewed composite has the stiffness about the circumference dominated by the matrix, which transitions to the rubbery region at 125°C, does not show good agreement in the rubbery region. Therefore, extrapolating glassy region mechanical material properties to the rubbery region for non-aligned geometries is not sufficient to capture the behavior in the rubbery region.

Taking a moment to disregard the experimental results and simply comparing the results from the temperature dependent and independent models. Both material models are nearly on top of each other and only have minimal differences. The temperature dependent model follows the trends of the experimental results more closely with regards to the smooth transition between the glassy and rubbery region slopes (rather than the disjoint results from the temperature independent model). This one aspect, however, is less significant to the fact that the temperature dependent model requires many more input parameters. Temperature dependent material models either require additional testing (monetarily and temporally expensive) or assumptions (greater uncertainty) as compared to the temperature dependent models. The temperature dependent models perform just as well as the temperature dependent models and, therefore, will be the material model that is used for the uncertainty quantification studies.

Although there are measurable differences between the simulated and experimental results, the comparisons shown in the figures above are adequate to permit the model's use in further studies of model parameter sensitivity and uncertainty quantification. Furthermore, since it has been postulated that the measurable differences demonstrated in the above figures are related to uncertainty in the parameters defining the composite material's elastic behavior, the bi-material split ring finite element model definition would benefit from the thorough examination of the effects of material property uncertainty on the predicted residual stress response.

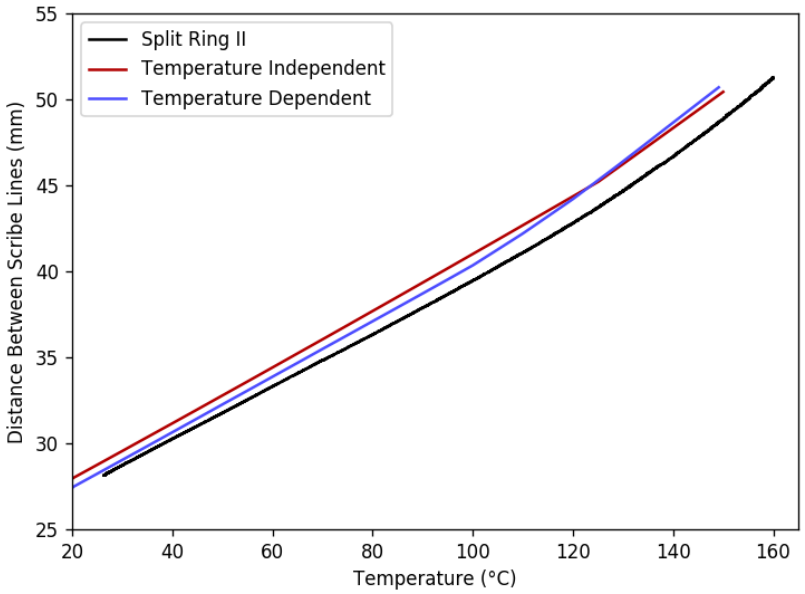

Figure 4.5: Comparison of temperature dependent and independent simulations with the experiment: carbon fiber composite (no skew).

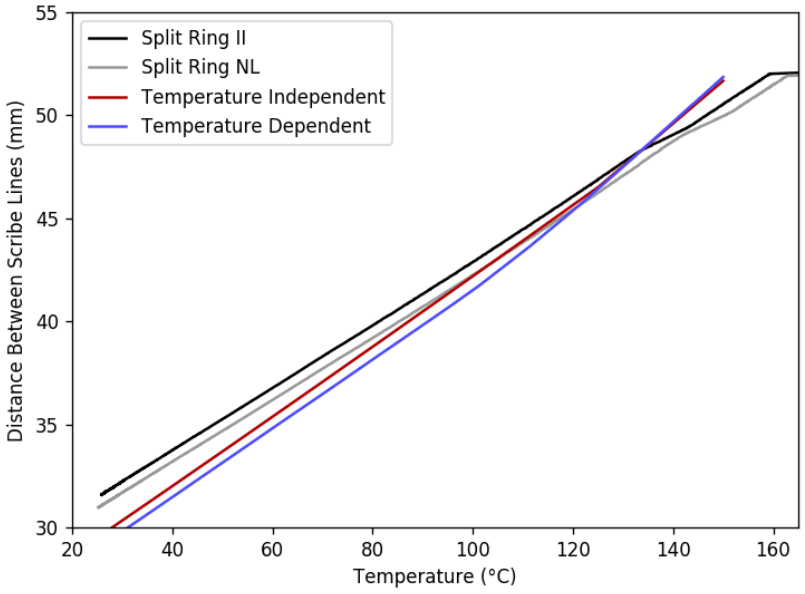

Figure 4.6: Comparison of temperature dependent and independent simulations with the experiment: carbon fiber composite (45° skew).

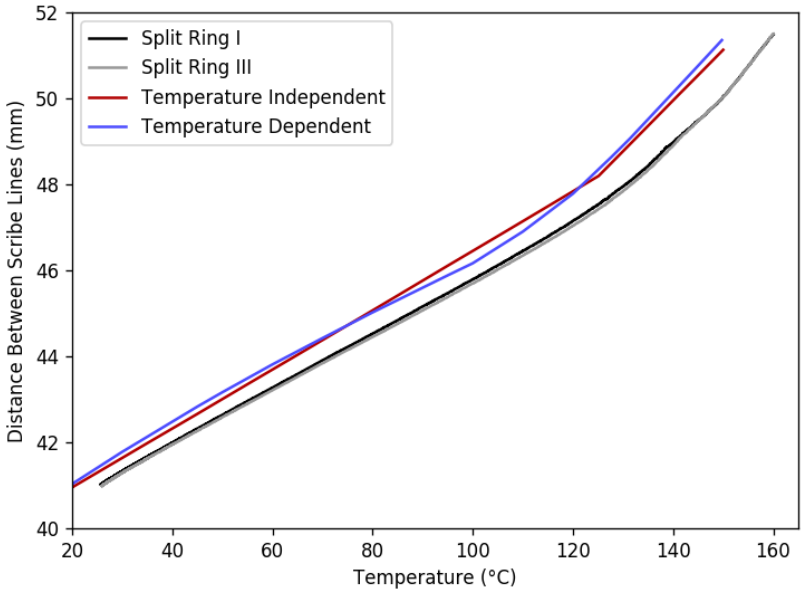

Figure 4.7: Comparison of temperature dependent and independent simulations with the experiment: glass fiber composite (no skew).

Chapter 5

Uncertainty Quantification

The results of the nominal simulations in the previous chapter are in agreement with the experimental results, but do not perfectly agree. It is unreasonable to think that perfect agreement would exist between the simulated and experimental results as the parameters describing the material models and geometry of the simulation are not known with 100% certainty. Instead of defining these parameters by their means, they can be defined by distributions, which then can be used to generate a range of possible values that can then be compared to the experiments. Determining this range, or quantifying the uncertainty, is a two step process: first, the parameters that influence the results (in this case, the residual stress state) are identified and then those parameters are given distributions in order to provide a range of simulation results. The following sections give the details of this process.

5.1 Parameter Distributions

The entire basis of quantifying the uncertainty in the simulations is based on accurate parameter distributions. Therefore, when possible, the distributions were defined as accurately as possible from experiments, measurements, or literature. The basis for each parameter, measured or inferred, considered in the simulations is defined below.

5.1.1 Geometry Parameters

There are five geometric parameters that were needed to fully specify the bi-material split ring geometry: inner diameter, aluminum thickness, total thickness, ring width, and the width of the removed sector. The width of the removed sector has no consequence as the the experimental measurements were taken at scribe lines on the composite face of the split ring (the removed sector purely allows the residual stress to become visible). The ring width is sufficiently large to prevent edge effects of the split ring to interfere with the measurement of the scribe lines at the mid plane. Therefore, only three geometric parameters were considered in the sensitivity study and required parameter distributions.

Aluminum Pipe Inner Diameter

As stated in Section 2.1, the inner diameter of pipes is not a defined dimension. Therefore, the minimum and maximum inner diameters were calculated from the outer diameter (114.3 mm), wall thickness (3.048 mm), and their tolerances. The tolerance for the outer diameter of a number 4 pipe, schedule 10 is ± 0.7874 mm) and the tolerance for wall thickness is ± 12.5% (± 0.381 mm). The resulting minimum and maximum inner diameters are given in Table 5.1 below.

Table 5.1: Parameter bounds for the inner diameter of the aluminum pipe.

Minimum ID (mm)	Nominal ID (mm)	Maximum ID (mm)
106.655	108.204	109.753

Due to the nature of the tolerances and the lack of physical measurements, the distribution of the inner diameter is defined as a uniform distribution with the limits given in Table 5.1.

Aluminum Thickness

In order to accommodate the use of a vacuum bag during the cure process, the aluminum pipe was sized to be four inches longer that the composite. This allowed the thickness of the aluminum to be measured at the top and bottom of the bi-material cylinder (Figure 5.1. The measurements are shown in Table 5.2.

Table 5.2: Aluminum thickness measurements (mm).

	CFRP (no skew)		CFRP (45° skew)		GFRP (no skew)	
Position	Top	Bottom	Top	Bottom	Top	Bottom
1	1.76	1.75	1.81	1.86	1.92	1.99
2	1.83	1.83	1.97	1.99	1.79	1.99
3	2.00	2.00	1.84	1.88	1.88	1.97
4	2.03	2.02	1.97	1.92	1.85	1.88
5	2.02	2.02	1.93	1.86	1.70	1.67
6	1.87	1.91	1.95	1.96	1.81	1.80
7	1.71	1.71	1.96	1.93	1.86	1.80
8	1.84	1.84	1.80	1.90	1.94	1.84

The thickness of the aluminum is not uniform about the circumference (Figure 5.2); however, the thickness follows the same circumferential trend at both ends. It would be too difficult to model aluminum with a varying thickness, so a mean value will be used. However, since the aluminum thickness was not measured in the region that the split rings were fabrication from, the measurements from the top and the bottom were used. In order to give confidence that the mean thickness of the aluminum remains constant along the length of the bi-material

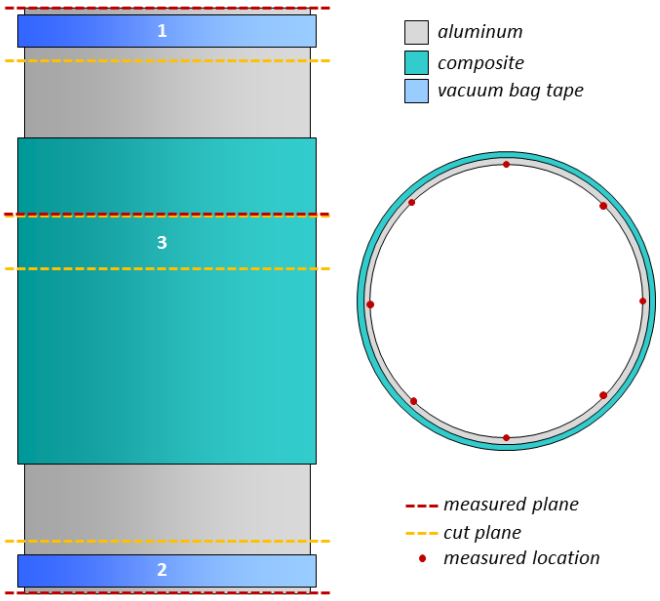

Figure 5.1: Measurement locations for aluminum thickness (1 and 2) and total thickness (3).

cylinder (i.e. the measurements at the top and bottom are adequate for determining the thickness of the aluminum of the split ring geometries), the measurements underwent a T-test. The T-test assesses the distributions of two samples against the null hypothesis that the two samples have the same mean. If the null hypothesis is retained (a p-value greater than 0.05), it can be said that it is possible that the two samples share the same mean.

The T-tests for all three split ring variants resulted in p-values greater than 0.05 (0.49 for the carbon fiber composite (no skew), 0.39 for the carbon fiber composite (45° skew), and 0.32 for the glass fiber composite (no skew)). Therefore, both the top and bottom samples were used to generate distributions for the bi-material split rings (Table 5.3). Since all aluminum for all the bi-material cylinders were machined separately, a different aluminum thickness was specified for each split ring.

Table 5.3: Aluminum thickness normal distributions and bounds (mm).

Composite	**Mean**	**Std.**	**Lower Bound[1]**	**Upper Bound[1]**
CFRP (no skew)	1.883	0.119	1.527	2.239
CFRP (45° skew)	1.908	0.060	1.728	2.088
GFRP (no skew)	1.856	0.094	1.573	2.138

[1]Lower and upper bounds calculated from: $\mu \pm 3\sigma$

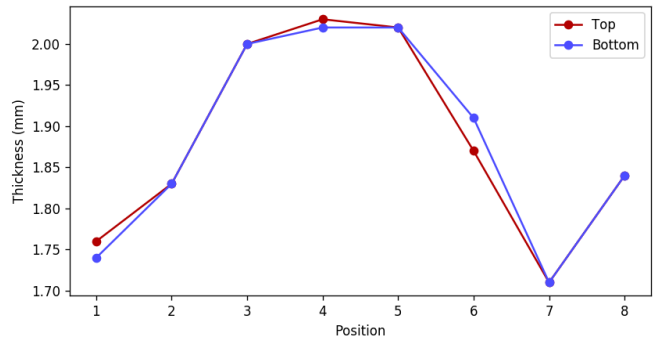

(a)

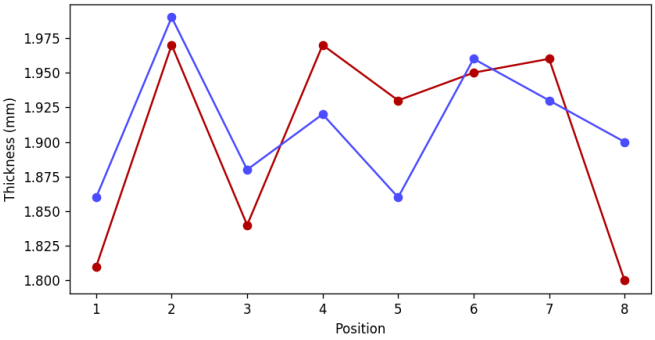

(b)

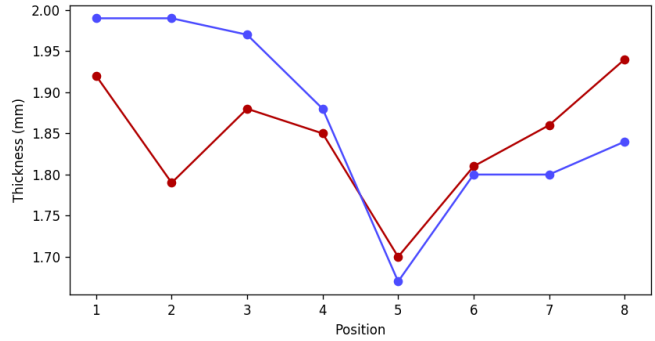

(c)

Figure 5.2: Measured aluminum thicknesses: (a) CFRP (no skew), (b) CFRP (45° skew), and (c) GFRP (no skew).

Total Thickness

The total thickness was measured in the same manner as the aluminum thickness. The measurements were taken from a bi-material ring that was measured before it was machined to a split ring (Figure 5.1). Table 5.4 gives the measurements and Table 5.5 gives the distribution and upper and lower bounds.

Table 5.4: Total thickness measurements and approximate composite thicknesses (mm).

	CFRP (no skew)		CFRP (45° skew)		GFRP (no skew)	
Position	**Total**	**Composite[1]**	**Total**	**Composite[1]**	**Total**	**Composite[1]**
1	3.19	1.44	3.33	1.50	3.33	1.38
2	3.27	1.44	3.60	1.62	3.34	1.45
3	3.49	1.49	3.46	1.60	3.38	1.46
4	3.52	1.50	3.42	1.48	3.23	1.37
5	3.51	1.52	3.48	1.59	3.28	1.60
6	3.43	1.54	3.38	1.43	3.37	1.57
7	3.26	1.55	3.48	1.54	3.41	1.58
8	3.34	1.50	3.49	1.64	3.39	1.50

[1]The composite thickness was calculated by subtracting the average aluminum thickness of the corresponding position.

Table 5.5: Total thickness normal distributions and bounds (mm).

Composite	**Mean**	**Std.**	**Lower Bound[1]**	**Upper Bound[1]**
CFRP (no skew)	3.380	0.133	2.981	3.779
CFRP (45° skew)	3.455	0.0.081	3.212	3.698
GFRP (no skew)	3.341	0.0.061	2.876	3.523

[1]Lower and upper bounds calculated from: $\mu \pm 3\sigma$

5.1.2 Aluminum Mechanical Properties

The mechanical properties of aluminum are well documented in literature and were assumed to vary very little, as shown in Table 5.6. The CTE of aluminum, on the other hand, was assumed to vary between two average CTEs (-50°C to 20°C and 20°C to 200°C) given by Table TE-2 of the ASME BPVC [12].

Table 5.6: Aluminum mechanical property distributions and bounds.

Property	**Mean**	**Std.**	**Lower Bound[1]**	**Upper Bound[1]**
E (GPa)	69.0	0.7	68.3	69.7
ν	0.33	0.003	0.327	0.333
CTE[2] (K^{-1})	-	-	21.8e-06	24.5e-06

[1]Lower and upper bounds calculated from: $\mu \pm 3\sigma$
[2]The bounds for the CTE were not based on standard deviations.

5.1.3 Composite Mechanical Properties

Uncertainty for the composite mechanical properties were only determined for the variables that were defined by testing (not micro mechanical modeling). These included E_{11}, E_{22}, G_{12}, and ν_{12}. The uncertainty for E_{33} was scaled from E_{22} due to the difference in magnitudes, where as G_{13} and G_{23} maintained the same uncertainty as G_{12} since their magnitudes are similar. All Poisson's ratios also used the same uncertainty. The distribution for T_g was determined from measurements taken during a thermomechanical analysis (TMA). Table 5.7 and 5.8 give the distributions and bounds for carbon fiber and glass fiber composites, respectively.

Table 5.7: Carbon fiber composite mechanical property normal distributions and bounds.

Property	**Mean**	**Std.**	**Lower Bound[1]**	**Upper Bound[1]**
E_{11} (GPa)	63.86	0.240	56.66	71.06
E_{11} (GPa)	62.74	0.236	55.67	69.81
E_{11} (GPa)	8.59	0.032	7.61	9.56
ν_{12}	0.048	0.0065	0.029	0.068
ν_{12}	0.408	0.0065	0.389	0.428
ν_{12}	0.408	0.0065	0.388	0.427
G_{11} (GPa)	3.44	0.11	3.11	3.77
G_{11} (GPa)	3.27	0.11	2.94	3.60
G_{11} (GPa)	3.25	0.11	2.92	3.58
T_g[2] (°C)	125.14	7.19	110.90	141.80

[1]Lower and upper bounds calculated from: $\mu \pm 3\sigma$
[2]The bounds for T_g were defined based on the observed upper and lower bounds.

Table 5.8: Glass fiber composite mechanical property normal distributions and bounds.

Property	**Mean**	**Std.**	**Lower Bound[1]**	**Upper Bound[1]**
E_{11} (GPa)	24.75	1.67	19.73	29.77
E_{11} (GPa)	23.10	1.02	20.03	26.16
E_{11} (GPa)	9.72	0.43	8.43	11.01
ν_{12}	0.13	0.0099	0.10	0.16
ν_{12}	0.36	0.0099	0.33	0.39
ν_{12}	0.36	0.0099	0.33	0.39
G_{11} (GPa)	3.48	0.11	3.15	3.81
G_{11} (GPa)	2.94	0.11	2.61	3.27
G_{11} (GPa)	2.94	0.11	2.61	3.27
T_g[2] (°C)	109.74	8.33	90.39	131.53

[1]Lower and upper bounds calculated from: $\mu \pm 3\sigma$
[2]The bounds for T_g were defined based on the observed upper and lower bounds.

5.1.4 Composite Coefficients of Thermal Expansion

Multiple measurements of the CTEs presented in Seciton 3.5.5 were taken at each temperature, which gives a normal distribution for each point in Figures 3.5 through 3.10. Using the distributions, upper and lower bound (based on $\pm\sigma$) temperature dependent CTEs can be plotted and used to compute the upper and lower bound average CTEs (Figures 5.3 through 5.8). Then, by dividing the difference between the lower bound and average CTE calculated in Section 3.5.5 by three, a standard deviation for the average CTEs was generated.

Table 5.9: Carbon fiber composite CTE normal distributions and bounds (1.0^{-6} K^{-1}).

Parameter	**Mean**	**Std.**	**Lower Bound[1]**	**Upper Bound[1]**
11 Glass	3.15	0.10	2.84	3.46
11 Rubber	0.95	0.16	0.46	1.45
22 Glass	3.62	0.09	3.37	3.88
22 Rubber	2.18	0.01	2.15	2.21
33 Glass	63.7	0.23	63.0	64.4
33 Rubber	228.5	1.55	223.8	233.1

[1]Lower and upper bounds calculated from: $\mu \pm 3\sigma$

Table 5.10: Carbon fiber composite CTE normal distributions and bounds (1.0^{-6} K^{-1}).

Parameter	**Mean**	**Std.**	**Lower Bound[1]**	**Upper Bound[1]**
11 Glass	14.32	0.17	13.80	14.84
11 Rubber	11.30	0.42	10.05	12.56
22 Glass	14.95	0.19	14.38	15.53
22 Rubber	13.50	0.47	12.08	14.92
33 Glass	58.9	0.63	57.0	60.8
33 Rubber	236.2	3.86	224.6	247.9

[1]Lower and upper bounds calculated from: $\mu \pm 3\sigma$

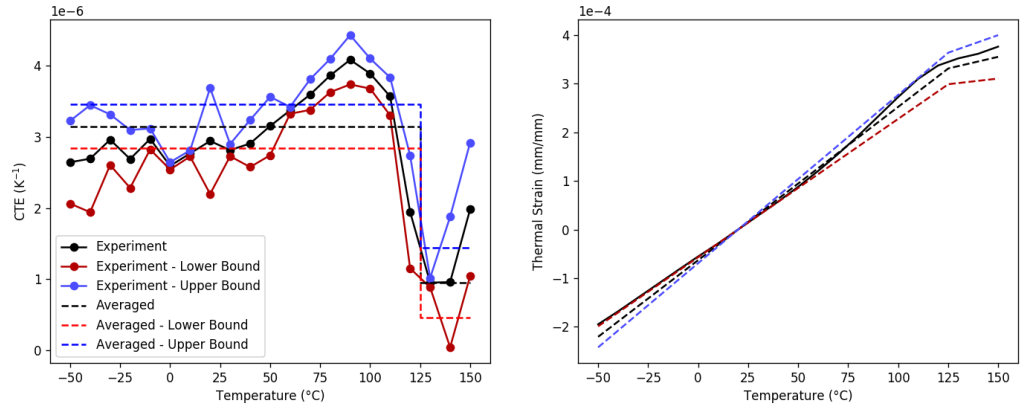

Figure 5.3: Upper and lower bounds of the averaged 11 direction CTE for the carbon fiber composite.

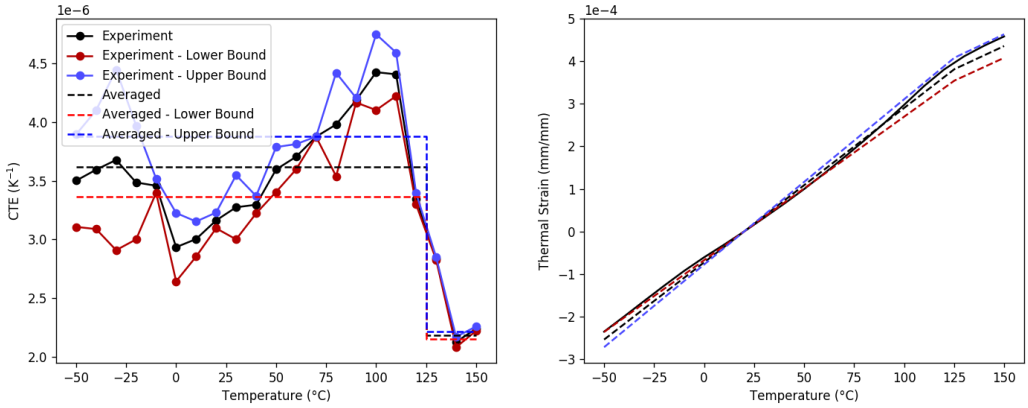

Figure 5.4: Upper and lower bounds of the averaged 22 direction CTE for the carbon fiber composite.

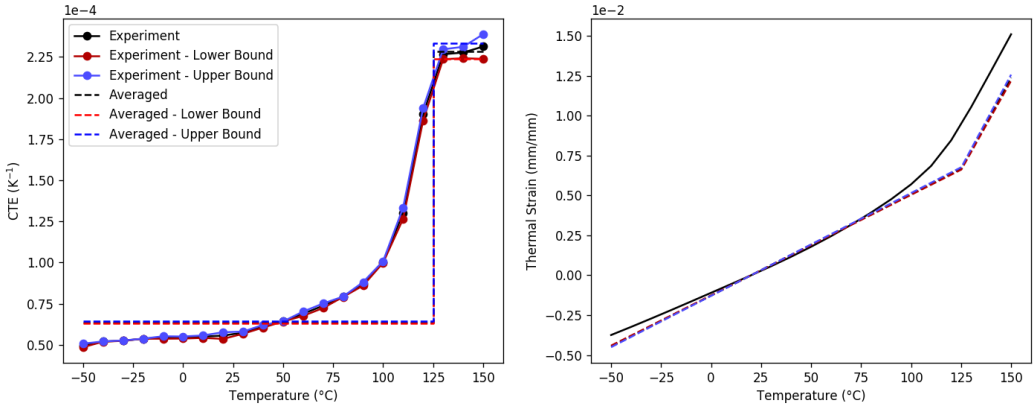

Figure 5.5: Upper and lower bounds of the averaged 33 direction CTE for the carbon fiber composite.

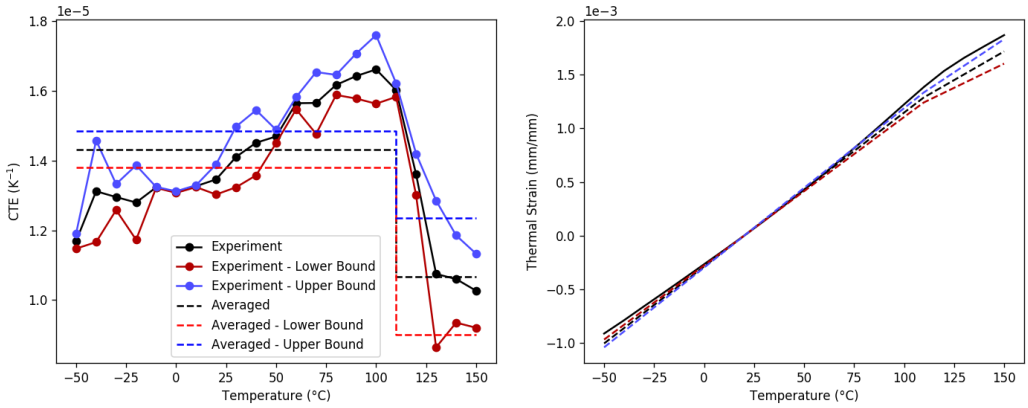

Figure 5.6: Upper and lower bounds of the averaged 11 direction CTE for the glass fiber composite.

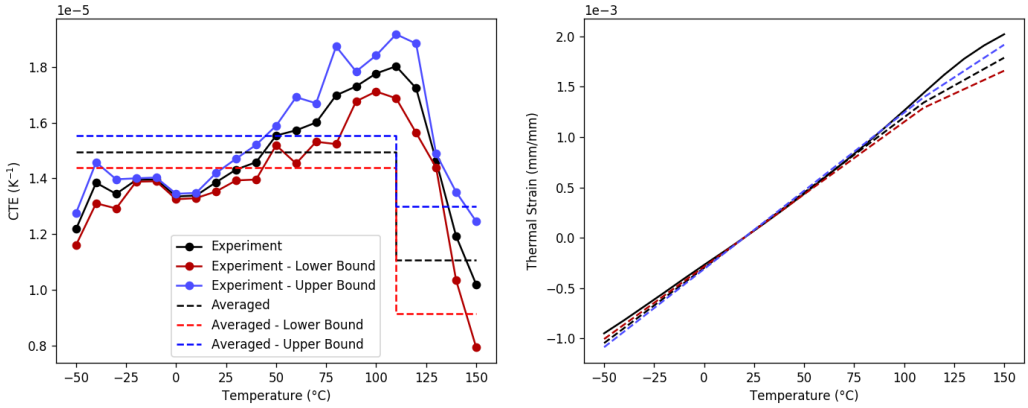

Figure 5.7: Upper and lower bounds of the averaged 22 direction CTE for the glass fiber composite.

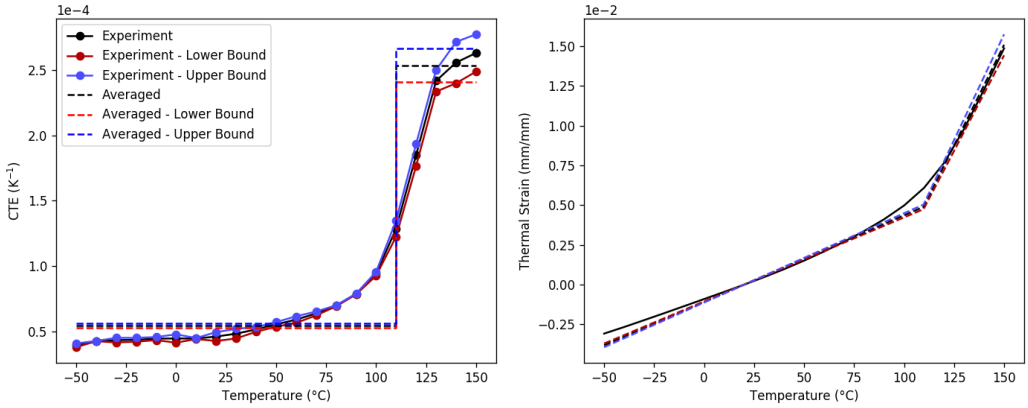

Figure 5.8: Upper and lower bounds of the averaged 33 direction CTE for the glass fiber composite.

5.1.5 Stress Free Temperature

The distributions for the stress free temperature were calculated using values from additional experiments outside those described in Table 2.3. Different experiments produced significantly different means for the stress free temperature, which results in a large variance for the distribution. This reflects a low confidence in the methodology currently used and indicates that a more accurate method for determining the stress free temperature needs to be investigated. Table 5.11 gives the distributions and upper and lower bounds for the stress free temperatures for both aluminum/carbon fiber composite and aluminum/glass fiber composite.

Table 5.11: Stress free temperature distribution and bounds.

Composite	**Mean**	**Std.**	**Lower Bound[1]**	**Upper Bound[1]**
CFRP[2]	147.37°C	4.30°C	134.46°C	160.28°C
GFRP	150.25°C	6.08°C	132.00°C	168.49°C

[1]Lower and upper bounds calculated from: $\mu \pm 3\sigma$
[2]CFRP with and without ply skew were combined in determining the stress free temperature distribution and bounds.

5.2 Input Parameter Sensitivity Study

From the previous sections, the bi-material split ring geometry is governed by three independent variables, the composite material properties are governed by sixteen, and the aluminum material properties are governed by three. Including the stress free temperature (which is a property of both the composite and aluminum), gives a total of twenty-three independent variables. Ideally, the uncertainty of all twenty-three parameters would be determined and not estimated; however, it is time and cost prohibitive to do so. Therefore, a sensitivity study is used to determine those parameters that have a significant influence on the residual stress state of the bi-material split ring.

5.2.1 Sensitivity Study Methods

All model parameters described in the previous section (Section 5.1) were considered to be potentially influential to the residual stress state of the bi-material split ring. The 23 parameters describe the constitutive models for both the composite material and the aluminum alloy as well as the geometry of the split ring (Table 5.12). Error in the placement of the fiber orientation of the composites, skew, was not considered in the sensitivity study due to the increased complexity needed in the finite element model (e.g. full symmetry would be required). Ply skew is known to have an effect on the residual stress state (the differences

between the carbon fiber composite without skew and with 45° skew demonstrate this); however, the error is assumed to be small (less than 2.5°) and the corresponding influence on the residual stress state is assumed to be much smaller than that of the stress free temperature, layer thickness, and CTEs.

Table 5.12: Model parameters considered during the sensitivity analysis.

Composite Mechanical Parameters
E_{11}, E_{22}, E_{33}
ν_{12}, ν_{13}, ν_{23}
G_{12}, G_{13}, G_{23}
CTE_{11}, CTE_{22}, CTE_{33} (glassy)
CTE_{11}, CTE_{22}, CTE_{33} (rubbery)
T_g
T_{sf}
Aluminum Mechanical Properties
E
ν
CTE
Geometric Parameters
Aluminum Inner Diameter
Aluminum Thickness
Total Thickness

The technique selected to sample the parameter space was representative and organized, such that a minimum number of sample sets and simulations could be used to develop and recognize trends and relationships between the 23 individual input parameters and the simulated residual stress output. Specifically, there are many different approaches that can be taken to efficiently sample a high dimensional parameter space. One such approach is the Box Behnken Design method. This approach, which was selected for the current sensitivity analysis, offers a highly stable sampling method. Particularly, the Box Behnken methodology avoids overly extreme parameter combinations as it does not sample outside of the defined process, or parameter, space. The parameter space of the 23 parameters was defined using the upper and lower bounds that represent plausible parameter values presented in Section 5.1. In addition to improved stability, when compared to other sampling approaches, the Box Behnken method also seems to require fewer overall samples to develop trends between the input parameters and the output. The relationship between the number of computer experiments designed with the Box Behnken approach and k potential input parameters can be expressed as:

$$N = 2k(k-1) + 1 \tag{5.1}$$

where N is the number of experiments, or simulations, and k is the number of parameters [14]. The Sandia developed toolkit, Dakota, was used to create the N simulations and managed

their submission [15]. Upon completion of the 1,013 simulations, the individual parameter sensitivities can be assessed with a multi-way analysis of variance (ANOVA). Specifically, the ANOVA represents a model independent, probabilistic sensitivity analysis method that can be used to determine the existence of statistical associations between an output response and one or more input parameters [16].

5.2.2 Sensitivity Study Results

The Box Behken design method was used to define 1,013 unique simulations for each of the split ring variants (for a total of 3,039 simulations). The simulations were processed with Sierra Adagio in the same manner as the nominal simulation, except that the fourth step of re-heating the split ring that was used to match the experiments was not included. Therefore, the sensitivity study used the residual stress state at room temperature, as measured by the distance between the two scribe lines to determine the influence of each parameter. At the conclusion of all the simulations, a multi-way ANOVA was applied to determine the influence of a parameter at a 5% significance level (i.e. $p = 0.05$). Tables 5.13 through 5.15 indicate the significant parameters and Figures 5.9 through 5.11 show the main effects plot. The main effects plot gives a visual representation to the significance of each parameter - if a parameter has a noticeably non-zero slope, it is significant. It also shows the relationship of the parameter to the residual stress state (positive vs. negative slope) and provides a simple way to gauge relative sensitivity of parameters (a greater slope equates to greater significance).

The carbon fiber composite split ring without skew showed eleven sensitive parameters, with skew gave sixteen, and the glass fiber composite gave twelve. All the parameters identified affect the stiffness of the split ring or the thermal expansion about the circumference of the split ring, which is logical. Of all the composite material properties identified as influential, only G_{23} for the carbon fiber composite was not experimentally determined. Other non-experimentally determined properties were all the aluminum mechanical properties (E, ν, and CTE) and the inner diameter of the aluminum pipe. The CTE for aluminum is the only parameter of the five that presents a significant influence on the residual stress state, therefore, the uncertainty quantification in the subsequent section will be driven mostly by measured values.

Table 5.13: Carbon fiber composite (no skew) split ring sensitive parameters (in red).

Composite Mechanical Parameters
E_{11}, E_{22}, E_{33}
ν_{12}, ν_{13}, ν_{23}
G_{12}, G_{13}, G_{23}
CTE_{11}, CTE_{22}, CTE_{33} (glassy)
CTE_{11}, CTE_{22}, CTE_{33} (rubbery)
T_g
T_{sf}
Aluminum Mechanical Properties
E
ν
CTE
Geometric Parameters
Aluminum Inner Diameter
Aluminum Thickness
Total Thickness

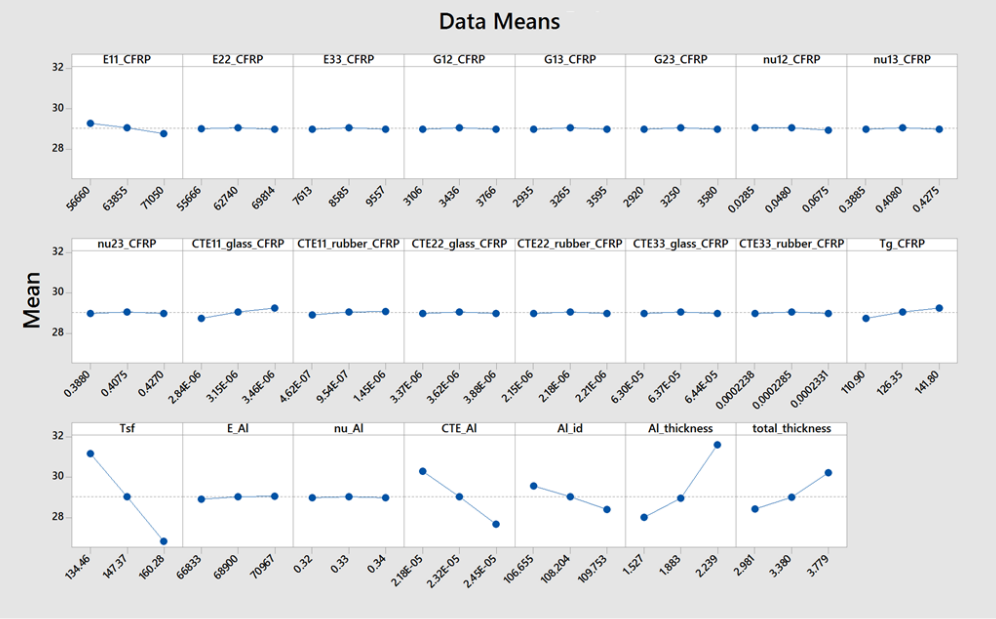

Figure 5.9: Main effects plot for the carbon fiber composite (no skew) split ring.

Table 5.14: Carbon fiber composite (45° skew) split ring sensitive parameters (in red).

Composite Mechanical Parameters
E_{11}, E_{22}, E_{33}
ν_{12}, ν_{13}, ν_{23}
G_{12}, G_{13}, G_{23}
CTE_{11}, CTE_{22}, CTE_{33} (glassy)
CTE_{11}, CTE_{22}, CTE_{33} (rubbery)
T_g
T_{sf}
Aluminum Mechanical Properties
E
ν
CTE
Geometric Parameters
Aluminum Inner Diameter
Aluminum Thickness
Total Thickness

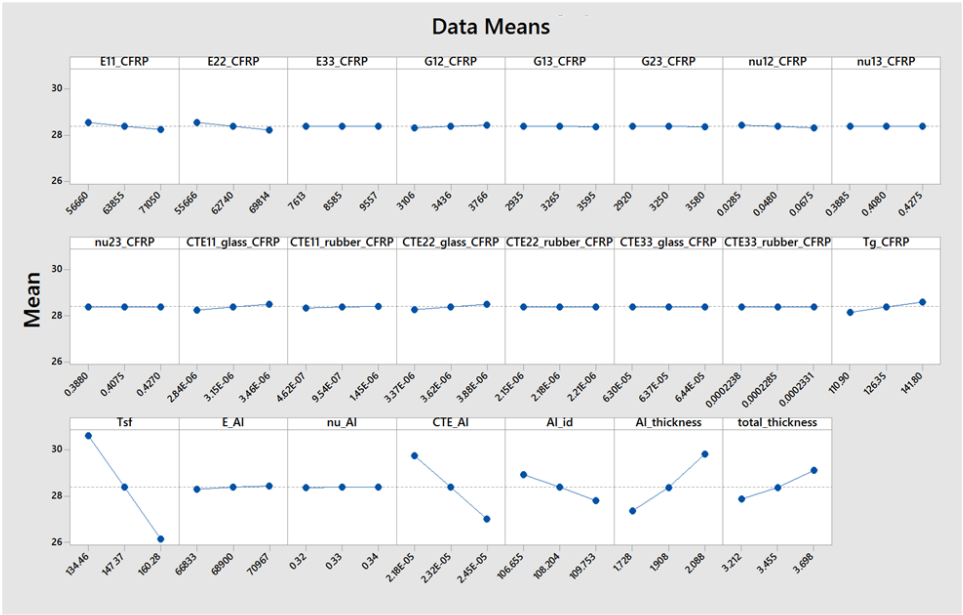

Figure 5.10: Main effects plot for the carbon fiber composite (45° skew) split ring.

Table 5.15: Glass fiber composite (no skew) split ring sensitive parameters (in red).

Composite Mechanical Parameters
E_{11}, E_{22}, E_{33}
ν_{12}, ν_{13}, ν_{23}
G_{12}, G_{13}, G_{23}
CTE_{11}, CTE_{22}, CTE_{33} (glassy)
CTE_{11}, CTE_{22}, CTE_{33} (rubbery)
T_g
T_{sf}
Aluminum Mechanical Properties
E
ν
CTE
Geometric Parameters
Aluminum Inner Diameter
Aluminum Thickness
Total Thickness

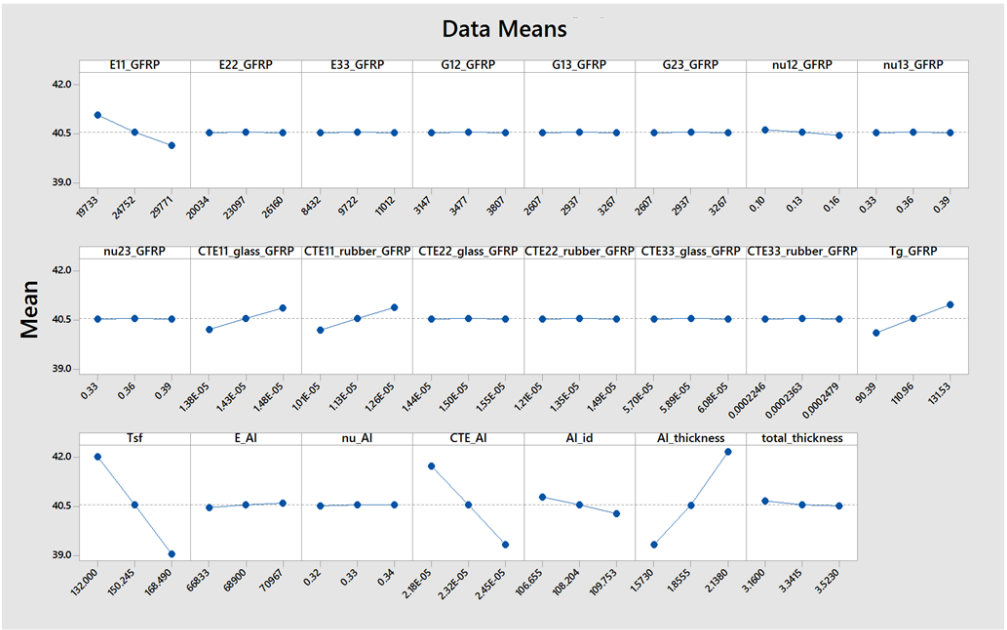

Figure 5.11: Main effects plot for the glass fiber composite (no skew) split ring.

5.3 Uncertainty Quantification

The final step in quantifying the uncertainty of the simulations samples a parameter space defined by the sensitive parameters determined in the previous section. The resulting samples will provide a range of plausible results for the residual stress state of the bi-material split rings based on the uncertainty of the individual parameters, which then are compared to the experimental results.

5.3.1 Uncertainty Quantification Methods

The uncertainty was quantified by sampling the parameter space created by the sensitive parameters and their distributions, which propagates the uncertainty of the individual input parameters to the output parameter, the residual stress state. The sampling was conducted using the latin hypercube sampling (LHS) method [17]. Instead of randomly sampling, LHS divides the n-dimensional space into n-dimensional 'cubes' and then samples from the regions such that the range of each parameter is represented in the sample set. Therefore, fewer samples using the LHS method (as apposed to random, monte carlo sampling) should be needed to achieve a converged distribution solution. As with the Box Behnken method for the sensitivity study, Dakota was used as the conduit to run LHS sampling on the parameter space and manage the simulations [15].

5.3.2 Uncertainty Quantification Results

The distributions of all the parameters are defined in Section 5.1, where all but the CTE of aluminum and the inner diameter of the aluminum pipe were given normal distributions (the aluminum inner diameter and CTE were given uniform distributions). For each split ring variant, the parameter space was sampled using the Latin Hypercube Sampling (LHS) method at sample sizes of 25, 50, and 100 (a total of 300 simulations across all three split rings), as shown in Figures 5.12 through 5.14. Table 5.16 gives the means and standard deviations for the residual stress state at room temperature for all sample sets, which indicate that 25 samples were sufficient to define the uncertainty bounds.

Table 5.16: Sample mean and standard deviation at room temperature.

	CFRP (no skew)		**CFRP (45° skew)**		**GFRP (no skew)**	
Sample Size	**Mean**	**Std.**	**Mean**	**Std.**	**Mean**	**Std.**
25	28.43	1.45	29.17	1.76	41.36	0.90
50	28.43	1.46	29.10	1.70	41.37	0.93
100	28.44	1.49	29.21	1.83	41.37	0.90

The uncertainty band for the carbon composite split ring encompasses the experimental data

(within or at the boundary), whereas the bounds only capture the glassy region of the glass composite split ring. Furthermore, the uncertainty region grows as the temperature departs from the stress free temperature, indicating that the results of the residual stress state are highly dependent on an accurate determination of the stress free temperature. Finally, as the sample size increases, the samples clearly develop a normal distribution (Figures 5.12-5.14). The final room temperature predictions of residual stress show that the experiments are within one standard deviation of the simulations for the no skew split rings and within two for the carbon fiber composite split ring with 45° skew (Table 5.17).

Table 5.17: Final predictions of the split ring room temperature residual stress state.

Split Ring	**Prediction (mm)**	**Experimental Mean (mm)**
CFRP (no skew)	28.43 ± 5.1%	28.14
CFRP (45° skew)	29.17 ± 6.0%	31.28
GFRP (no skew)	41.36 ± 2.2%	41.00

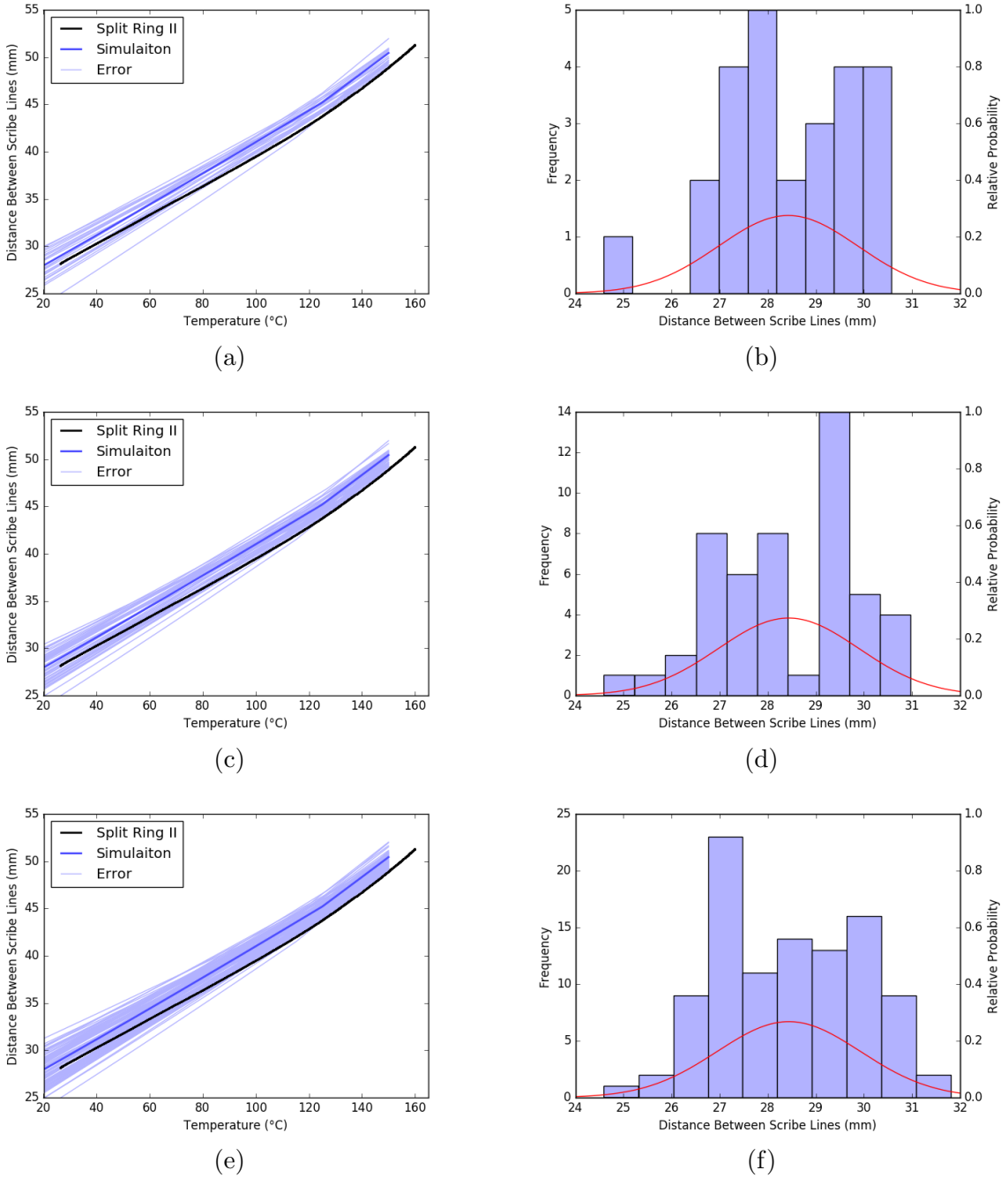

Figure 5.12: Carbon fiber composite (no skew) split ring sample sets (left) and distributions (right): 25 samples (a, b), 50 samples (c, d), and 100 samples (e, f).

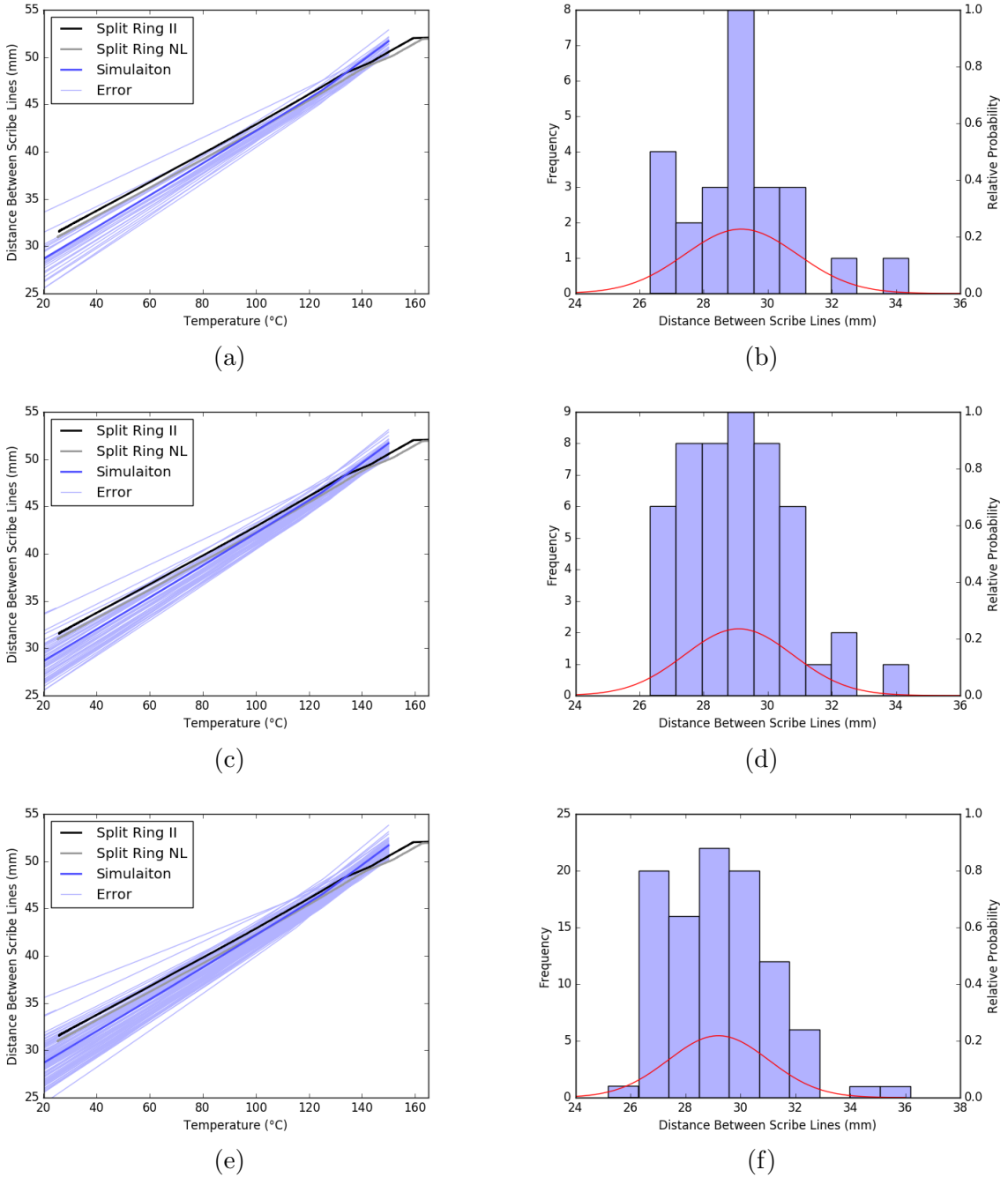

Figure 5.13: Carbon fiber composite (45° skew) split ring sample sets (left) and distributions (right): 25 samples (a, b), 50 samples (c, d), and 100 samples (e, f).

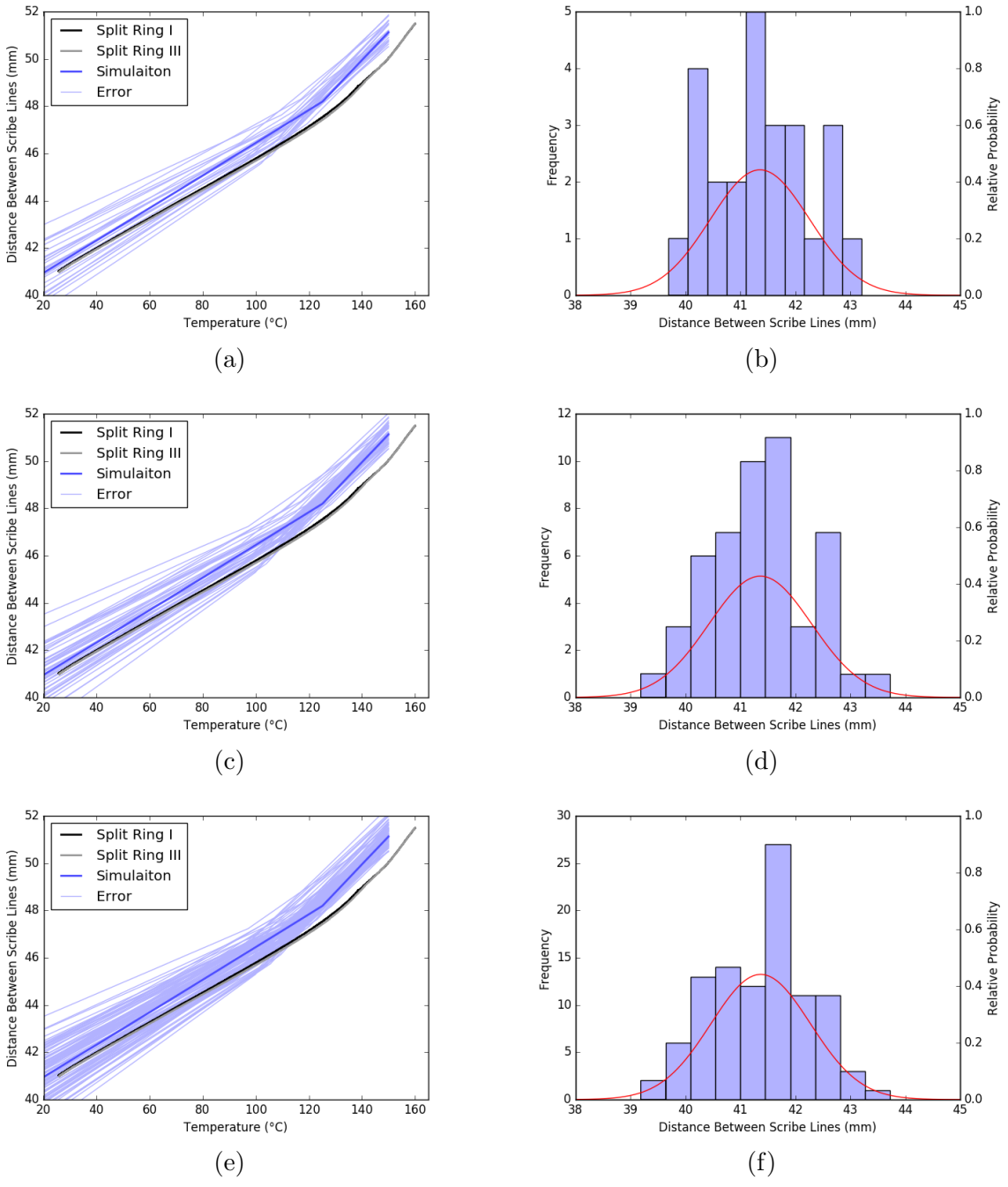

Figure 5.14: Glass fiber composite (no skew) split ring sample sets (left) and distributions (right): 25 samples (a, b), 50 samples (c, d), and 100 samples (e, f).

Chapter 6

Conclusion

6.1 Results and Conclusion

A simplified composite process modeling methodology was used to predict the residual stresses due to the composite curing process in split rings with different composites and orientations, which were then compared to experimentally determined displacements over a range of temperatures. The simulation methodology showed good agreement with the experiments for all materials and orientations, as well as for both the temperature independent and dependent material models. For temperatures below the glass transition temperature, the simulation shows better agreement with the experiments than temperatures greater than the glass transition temperature. Overall, several conclusions can be drawn:

- Extrapolating the temperature dependence into the rubbery region of the composite from experimental results solely in the glassy region is not sufficient to capture the behavior within the rubbery region. With that being said, inaccurate mechanical properties of the composite in the rubbery region have no bearing on the residual stress state in the glassy region since the analysis is elastic and has no path dependence. The composite properties related to the rubbery region that have an effect (coefficients of thermal expansion and the glass transition temperature) are measured from experiments and taken into account in the simulations.
- The temperature independent and dependent models remain within a few percent error of each other over the entire simulation in both the glassy and rubbery region of the composites. This indicates that a temperature independent model is sufficient in predicting the residual stress state of the bi-material split rings with a reasonable level of accuracy compared to the temperature dependent model. This also suggests that changing the behavior of the composites mechanical properties to be similar to that of the coefficients of thermal expansion of the temperature independent material model (partially temperature dependent with a single value for above and below the glass transition temperature) may improve the results in the rubbery region of the composite. However, these material properties should be experimentally determined and not extrapolated from lower temperature experiments.
- The simulation error is not constant over the examined range of temperatures and increases as the temperature deviates from the stress free temperature. This is an

indication that accurate definitions of the stress free temperature, the coefficients of thermal expansion, and the glass transition temperature are needed to reduce the uncertainty at lower temperatures as these parameters govern the placement and slope of the simulation.

6.2 Future Work

As the residual stress modeling methodology continues to be developed and verified and validated, there are options for future efforts. More specifically, in the region of verification and validation, efforts can be focused on better determination of parameters and the optimization of uncertainty quantification methods. Over 3,300 total runs for the split ring model has a relatively low computational cost; however many other models do not. Reducing the number of total runs or using surrogate models through different uncertainty quantification methods would greatly benefit the larger models than run for hours rather than minutes.

References

[1] Timoshenko S. Analysis of bi-metal thermostats. *Journal of the Optical Society of America*, 11:233–255, 1925.

[2] F. S. Jumbo, I. A. Ashcroft, A. D. Crocombe, and M. M. Abdel Wahab. Thermal residual stress analysis of epoxy bi-material laminates and bonded joints. *International Journal of Adhesion and Adhesives*, 30:523–538, 2010.

[3] S. R. White and H. T. Hahn. Process modeling of composite materials: Residual stress development during cure. part i. model formulation. *Journal of Composite Materials*, 26:2402–2422, 1992.

[4] S. R. White and H. T. Hahn. Process modeling of composite materials: Residual stress development during cure. part ii. experimental validation. *Journal of Composite Materials*, 26:2423–2453, 1992.

[5] B. Tavakol, R. Roozbehjavan, A. Ahmed, R. Das, R. Joven, H. Koushyar, A. Rodriguez, and B. Minaie. Prediction of residual stresses and distortion in carbon fiber-epoxy composite parts due to curing process using finite element analysis. *Journal of Applied Polymer Science*, pages 941–950, 2013.

[6] B. L. Volk, M. Braginsky, Hoosm K., E Iarve, D. Mollenhauer, and T. Storage. Predicting the open hole tension of organic matrix composites incorporating the effects of processing. In *CAMX Conference Proceedings*, Dallas, TX, October 2015. CD-ROM.

[7] B. L. Volk, S. M. Nelson, A. A. Hanson, T. M. Briggs, T. Storage, and B. T. Werner. Evaluation of process modeling methodologies for out-of-autoclave polymer matrix composites. In *CAMX Conference Proceedings*, Anaheim, CA, September 2016. CD-ROM.

[8] A. A. Hanson, S. M. Nelson, B. T. Briggs, T. M. Werner, B. L. Volk, and T. Storage. Experimental measurement and finite element modeling of residual stresses in simple composite structures. In *CAMX Conference Proceedings*, Anaheim, CA, September 2016. CD-ROM.

[9] H. T. Hahn. Residual stresses in polymer matrix composite laminates. *Journal of Composite Materials*, 10:266–278, 1976.

[10] SIERRA Solid Mechanics Team. Sierra/SolidMechanics 4.44 User's Guide. Technical report (UUR) SAND2017-4016, Sandia National Laboratories, Albuquerque, New Mexico 87185 and Livermore, California 94550, April 2017.

[11] Stacy Nelson, Alexander Hanson, Timothy Briggs, and Brian Werner. SIERRA/SolidMechanics Modeling of Residual Stresses in Simple Composite Structures. Technical report (UUR) SAND2016-11807, Sandia National Laboratories, Livermore, California 94550, November 2016.

[12] ASME Boiler and Pressure Vessel Committee on Materials. 2017 ASME Boiler and Pressure Vessel Code, Section II Materials, Part D Properties (Metric). International Code ASME BPVC.II.D.M-2017, ASME, New York, New York 10016, July 2017.

[13] P. J. Roache. Perspective: A method for uniform reporting of grid refinement studies. *Journal of Fluids Engineering*, 116:405–413, 1994.

[14] S. Ferreira, R. Bruns, H. Ferreira, G. Matos, J. David, G. Brandao, E. Silva, L. Portigal, P. dos Reis, A. Souza, and W. dos Santos. Box-behnken design: An alternative for the optimization of analytical methods. *Analytica Chimica ACTA*, 597:179–186, 2007.

[15] institution= Sandia National Laboratories year= 2017 month= May type= Technical report (UUR) number= SAND2014-4633 address= Albuquerque, New Mexico 87185 Sandia National Laboratories Dakota Team (2017), title= akota, A Multilevel Parallel Object-Oriented Framework for Design Optimization, Parameter Estimation, Uncertainty Quantification, and Sensitivity Analysis: Version 6.6 Users Manual. Technical report.

[16] NIST/SEMATECH. e-Handbook of Statistical Methods. *http://www.itl.nist.gov/div898/handbook/*, 2013.

[17] W. Niccoli, F. Marinelli, T. Fairbanks, and R. Dancause. Latin hypercube sampling: Application to pit lake hydrologic modeling study. In *Conference on Hazardous Waste Research*, Snowbird, Utah, May 1998.

DISTRIBUTION:

1	MS 0840	J. Redmond, 1150
1	MS 9042	C. Nilsen, 8250
1	MS 9161	C. Mailhiot, 8340
1	MS 9153	C. Tewell, 8220
1	MS 9042	A. Brown, 8259
1	MS 9042	S. Peterson, 8343
1	MS 9106	A. Rowen, 8222
1	MS 9042	S. Nelson, 8259
1	MS 9042	A. Skulborstad, 8259
1	MS 9042	B. Werner, 8343
1	MS 9042	J. Huiqing, 8343
1	MS 9106	T. Briggs, 8222
1	MS 9042	S. Scheffel, 8222
1	MS 9403	C. Hagan, 8222
1	MS 0899	Technical Library, 9536 (electronic copy)


Sandia National Laboratories